# Deformation Mechanisms of NiAl Cyclicly Deformed Near the Brittle-to-Ductile Transformation Temperature

NASA Grant #NCC3-116

Final Report December 17, 1992

Prepared by:

Stephen D. Antolovich
Professor and Director
School of Materials Engineering
Mechanical Properties Research Laboratory
Georgia Tech

Ashok Saxena
Professor of Materials Engineering
Mechanical Properties Research Laboratory
Georgia Tech

Cheryl Cullers
Graduate Assistant
School of Materials Engineering
Mechanical Properties Research Laboratory
Georgia Tech

# INTRODUCTION

One of the ongoing challenges of the aerospace industry is to develop more efficient turbine engines. Greater efficiency entails reduced specific strength and larger temperature gradients, the latter of which means higher operating temperatures and increased thermal conductivity. Continued development of nickel-based superalloys has provided steady increases in engine efficiency and the limits of superalloys have probably not been realized. However, other material systems are under intense investigation for possible use in high temperature engines. Ceramic, intermetallic, and various composite systems are being explored in an effort to exploit the much higher melting temperatures of these systems.

NiAl is considered a potential alternative to conventional superalloys due to its excellent oxidation resistance, low density, and high melting temperature. The fact that NiAl is the most common coating for current superalloy turbine blades is a tribute to its oxidation resistance. Its density is one-third that a typical superalloys and in most temperature ranges its thermal conductivity is twice that of common superalloys. Despite these many advantages, NiAl requires more investigation before it is ready for use in engines. Binary NiAl in general has poor high-temperature strength and low-temperature ductility. On-going research in alloy design continues to make improvements in the high-temperature strength of NiAl. The factors controlling low temperature ductility have been identified in the last few years. Small, but reproducible ductility can now be achieved at room temperature through careful control of chemical purity and processing. But the mechanisms controlling the transition from brittle to ductile behavior are not fully understood. Research in the area of fatigue deformation can aid the development of the NiAl system in two ways. Fatigue properties must be documented and optimized before NiAl can be applied to engineering systems. More importantly though, probing the deformation mechanisms operating in fatigue will lead to a better understanding of NiAl's unique characteristics.

Low cycle fatigue properties have been reported on binary NiAl in the past year, yet those studies were limited to two temperature ranges; room temperature and near 1000 K. Eventually fatigue property data will be needed for a wide range of temperatures and compositions. The intermediate temperature range near the brittle-to-ductile transition was chosen for this study to ascertain whether the sharp change occurring in monotonic behavior also occurs under cyclic conditions. An effort was made to characterize the dislocation structures which evolved during fatigue testing and comment on their role in the deformation process.

# BACKGROUND

## Properties of NiAl

### Physical Metallurgy

Binary NiAl is an ordered intermetallic compound with a B2 crystal structure within the chemistry range of 45 to 60 atomic percent Ni at moderate temperatures. The B2 crystal structure is equivalent to two interpenetrating simple cubic structures with Ni atoms on one lattice and Al atoms on the other. The long-range order of NiAl in this phase, designated $\beta$ on the Ni/Al phase diagram, is maintained up to the melting temperature. An excellent review of $\beta$ NiAl has recently been written by Noebe, Bowman, and Nathal [1]. Material properties relevant to this study will be presented here.

Besides its high degree of order, some of the properties which stirred interest in NiAl as a high-temperature structural material include its high melting temperature, low density, and high thermal conductivity. The melting temperature for stoichiometric NiAl is 1911 K. The density of stoichiometric NiAl is approximately 5.90 g/cm$^3$ [2], with density increasing for additional Ni content and decreasing with additional Al content. For single crystal, stoichiometric NiAl the thermal conductivity is between 70 and 80 W/m-K [3]. Many of NiAl's properties are very sensitive to chemistry, especially near the equiatomic composition. Early x-ray diffraction studies found that in Ni-rich alloys Ni atoms substituted on the Al sublattice but that vacancies filled the Ni sites in Al-rich alloys [2].

Elastic properties have been determined for NiAl from acoustical techniques. Near stoichiometric NiAl has been found to have temperature dependent Young's modulus and shear modulus while Poisson's ratio had a much smaller temperature dependence. Tressler, Hellmann, and Hahn evaluated data and provided convenient estimates for elastic and shear moduli as well as Poisson's ratio [4]. One estimate of the temperature dependence of Young's modulus, E, of polycrystalline NiAl gives the following empirical relation for E in GPa and T in K:

$$E=204.9-0.041(T) \tag{2.1}$$

Tressler et at. give also an empirical relationship for the shear modulus:

$$G=76.6-0.017(T) \tag{2.2}$$

with the units again being GPa and K. Poisson's ratio can be calculated from the empirical E and G equations and is approximately equal to

$$\nu=0.307+2.15\times10^{-5} \tag{2.3}$$

Single crystal elastic stiffness constants were measured by Rusovic and Warlimont as a function of temperature and composition [5]. For a stoichiometric composition and near room temperature, the values they determined were approximately $C_{11}$ = 2.1x10$^{12}$ MPa, $C_{12}$

= $1.3x10^{12}$ MPa, and $C_{44}$ = $1.1x10^{12}$ MPa. These number lead to an anisotropy factor, $A = 2C_{44}/(C_{11}-C_{12})$ approximately equal to 3.

Early predictions of the operative slip system in CsCl structures, such as NiAl, based on atomic bond ordering energies suggest that <111> superdislocation would dominate slip in NiAl [6]. Concurrent with their own observations of <100> slip, Ball and Smallman used elastic energies of unit dislocations and dislocation dissociations to explain the predominance of <100> dislocations [7]. In polycrystalline NiAl and in most single crystal orientations, <100> {110} slip has been identified virtually exclusively. Single crystals oriented in <100> directions are
referred to as "hard" orientations since the resolved shear stress on <100> dislocations is zero. At low temperatures, room temperature and below, slip of <111> dislocations has been observed [8]. (When the strain rate is sufficiently high kinking is frequently observed and the geometrical reorientation leads to deformation along <100>.) Field, Lahrman, and Darolia have presented evidence that <110> dislocation gliding on {110} planes dominate the deformation of <100> oriented crystals at intermediate temperatures [9].

Mechanical Metallurgy

Mechanical property data on NiAl proved to be conflicting and widely misunderstood until fairly recently. The sensitivity of this system to compositional variations, vacancy concentrations, and impurity content was probably the reason for much of the confusion. Single and polycrystalline NiAl deform in a brittle fashion at ambient temperature and have a sharp transition to ductile behavior at intermediate temperatures. Ball and Smallman have shown [7], employing the technique utilized by Groves and Kelly [10], that glide and cross-glide of <100> dislocations on {110} planes provides only three independent slip systems. In 1928, von Mises demonstrated for the face centered cubic (FCC) system five independent slip systems were necessary to accommodate grain boundary deformation in polycrystalline materials. Although macroscopic abient temperature ductility can be achieved in NiAl tested in compression and to a limited extent in tension, this deformation is accomplished congruently with the opening of grain boundary cracks. True ductility is not achieved in polycrystalline NiAl until the brittle-to-ductile transition temperature (BDTT) of 500-600 K is reached. The BDTT is slightly lower in soft orientation single crystals.

The changes in mechanisms leading to the sharp transition in ductility have not been clearly isolated. The BDTT has been shown to be affected by, e.g., grain size, composition, impurity content, vacancy concentration, and deformation rate. Off-stoichiometric compositions and the high cooling rates associated with certain processing technique are major factors in determining the BDTT. Constitutional defects and quenched-in vacancies increase the yield strength and subsequently the BDTT. Additional active slip systems have not been confirmed above the BDTT, so an alternate process must occur. Several studies [7,11,12,13,14,15,16] have suggested that thermally assisted deformation, such as dislocation climb is activated. Groves and Kelly demonstrated that a combination of glide and climb of <100> dislocations provides five independent deformation mechanisms [17] which could accommodate grain-boundary strain. An *in situ* annealing study confirmed the activation of diffusive mechanisms on dislocations near grain boundaries at temperature corresponding to the BDTT of the material studied [16]. This explanation does not,

however, present the complete picture since there is also a sharp brittle-to-ductile transition in NiAl single crystals.

In addition to identifying the active slip system in NiAl, some comments have been made about the dislocation morphology. Researchers have identified the development of cellular arrays of dislocations after deforming polycrystalline NiAl to 1% strain in compression [16], and 2% in tension [18]. Nagpal and Baker [18] suggest this cell structure is the result of cross-slip which is fairly easy for stoichiometric NiAl and more difficult further from the stoichiometric composition.

## Fatigue Properties

### Fatigue of Metals

Fatigue is frequently the critical failure mode in structures subjected to thermal or mechanical loading. In general, structures exposed to macroscopic cyclical loading experience stress-controlled fatigue while parts subjected to thermal loading or the local areas around cracks and notches experience strain-controlled fatigue. Strain-controlled fatigue has become the more important mode from a design standpoint since manufactures seek use retirement-for-cause criterion rather than taking parts out of service based solely on number of cycles. That means using a part which contains cracks, but knowing how long the crack will remain sub-critical and not fail catastrophically. The area immediately surrounding a stress concentrator, whether it is a joint, notch or sub-critical size crack, deforms plastically but is enclosed by material deforming elastically. Thus the damage mechanism adjacent to the stress concentrator is plastic strain-controlled fatigue.

Early work in the fatigue area emphasized empirical relations and estimates for predicting life. Many of these estimates are indeed useful rules-of-thumb and can be used for comparing individual material responses to what is considered as the norm. If the unidirectional strain hardening exponent, n, is greater than 0.15 [19] (or greater than 0.2 [20]) cyclic hardening is expected. Fatigue life can be estimated by using strain to failure, $\epsilon_f$, to approximate the fatigue ductility coefficient in the Coffin/Manson power law function,

$$\frac{\Delta \epsilon_p}{2} = \epsilon_f' (2N_f)^c \qquad (2.4)$$

where $N_f$ is the number of cycles to failure and c is the fatigue ductility exponent. Life estimates can also be made using the Manson universal slopes equation, which is designed to include both ductility limiting low cycle fatigue and the strength limiting high cycle fatigue regimes using empirical constants and exponents, the ultimate tensile strength, $S_u$, and the Young's modulus, E.

$$\Delta \epsilon = 3.5 \frac{S_u}{E} (N)^{-0.12} + \epsilon_f^{0.6} (N)^{-0.6} \qquad (2.5)$$

Research delving into the internal deformation mechanisms of fatigue revealed many similarities with monotonic deformation. Slip planes and directions for a given material system are the same in unidirectional and cyclic testing [21]. Authors disagree on the extent to which deformation structures are parallel between the two test modes, but certain similarities have been established [22]. Fatigue damage in single phase FCC materials is concentrated in regions referred to as persistent slip bands (PSB). Persistent slip bands which intersect the specimen surface can be differentiated from other slip traces by careful polishing experiments. PSB development coincides with the advent of saturation in the cyclic stress-strain curve and the density of PSB increases with subsequent cycling. The dislocation structures associated with PSB are better understood for materials which deform by wavy slip than for those deforming by planar slip [23], but in general dislocation movement is not homogenous but is concentrated in the regions identified as ladder structures. The strain imposed during the fatigue test is accommodated by dislocation movement within the ladders and the matrix or bulk material experiences little activity. (Materials with second phases often show similar fatigue behavior, but will not be discussed in the context of this thesis.) The general PSB phenomenon has been observed to an extent in fatigue of some BCC materials [24,25], but effects have also been reported that do not occur in FCC fatigue [26,27].

Fatigue Research of NiAl

Before binary or alloyed, monolithic or composite, NiAl can be utilized as a structural material its fatigue properties must be characterized. Any limitations in fatigue strength or life will have to be understood and compensated for before NiAl can become a useful material system, in the strictest sense of the word useful. Obstacles in producing large, homogeneous heats of material and difficulty machining complicated specimens are some of the reasons which fatigue test programs have not been initiated until recently. Development of improved processing techniques along with understanding of monotonic properties, if not understanding of mechanisms, has given added value to the exploration of fatigue properties.

Room temperature and 1033 K fatigue tests were conducted by Bain et al. [28] on <100> single crystal NiAl-0.1% Mo. Tests were conducted in total strain control. Test scatter was minimal at the elevated temperature, but most initiation sites for room temperature tests were associated with pre-existing porosity in the crystals [29]. Secondary cracks, which coalesced and caused fast fracture, were observed parallel to the loading axis. The 1033 K cyclic lives compared favorably to the superalloy René N4 at high total strain ranges due to the larger ductility of NiAl. However at low total strain ranges, the NiAl crystals had shorter lives since the low yield strength of NiAl led to plastic deformation at strain ranges where René N4 remained elastic.

Room temperature cyclic tests have also been conducted by Hartfield-Wünsch [30,31] on $Ni_{49}Al_{31}Fe_{20}$ (which, like NiAl, deforms along <100> slip directions) at plastic strain ranges between 0.0004 and 0.01 and total strain rates between $3.4x10^{-5}$ and $10^{-4}$ $sec^{-1}$. The $Ni_{49}Al_{31}Fe_{20}$ fractured in a predominantly transgranular manner, experienced cyclic softening followed by hardening, and displayed little or no asymmetry between tensile and compressive portions of the load cycle.

Lerch and Noebe have performed room temperature [32] and 1000 K [33] fatigue tests on polycrystalline NiAl at plastic strain ranges between 0.0006 and 0.002 at a total strain rate of $10^{-3}$ $sec^{-1}$. At room temperature the polycrystalline NiAl tested in fatigue more sensitive to pre-existing flaws than identical material tested in tension. Unlike the single crystal material, which failed below its monotonic fracture stress, the polycrystalline specimens work hardened continuously at room temperature and failed at stresses averaging 60% higher than the monotonic fracture stresses. There was measurable asymmetry between the absolute value of the stresses achieved in tension and compression in these tests. The authors contributed the asymmetry to cracking within the specimens. The room temperature polycrystalline study found that in strain controlled fatigue NiAl had longer lives than other ordered B2 compounds. At 1000 K, polycrystalline NiAl experienced cyclic softening similar to the single crystal behavior. However, at the higher temperature polycrystalline NiAl reported suffered from grain boundary oxidation and creep cavitation.

Preliminary results have been published by Smith et al. on fatigue of <121> stoichiometric NiAl [34]. They report seeing evidence of persistent slip bands intersecting the specimen surface and dislocation structures similar to those resulting from monotonic testing. No mention was made of confirming that the surface slip bands observed were indeed continuously active or of the ladder dislocation structure indicative of typically wavy slip, FCC behavior.

General trends can be surmised from reported fatigue data. At low temperatures (room temperature is well below the BDTT for the materials discussed), NiAl cyclicly hardens and has little or no stable fatigue crack growth. Two of the groups [28,32] reported that fatigue fractures were initiated more frequently at pre-existing flaws than were the corresponding tensile fractures. At high temperatures, cyclic softening dominated the fatigue behavior of both single and polycrystalline NiAl. For polycrystalline NiAl, there was a two order of magnitude increase in fatigue lives from room temperature to 1000 K when tested at a plastic strain range of 0.002 [32,33]. Unfortunately, the dislocation structures developed during these previous studies have not been reported in detail. The properties reported at these two temperature extremes (one well below and one well above the BDTT) were quite different. This difference leads quite naturally to questioning the deformation behavior changes with increasing temperature.

## MATERIAL AND EXPERIMENTAL PROCEDURES

### Material and Metallographic Examination

A near stoichiometric NiAl billet was prepared by hot extrusion of vacuum atomized powders produced by Homogeneous Metals, Inc. Prealloyed -20/+325 mesh powders were extruded at 1365 K and a 3:1 reduction ratio. The composition of the extruded product is given in Table 3.1. The Al and Ni levels were determined by wet chemical analysis of triplicate samples.

Transverse and longitudinal metallographic sections were taken from the extrusion. Sections were mounted in bakalite, polished on standard grit paper wheels, and polished with 1 and 3 $\mu$m slurries on cloth wheels. Since NiAl is a hard, difficult to polish material, a special final polish was also used. A solution of 150 ml $H_2O$, 150 ml colloidal silica, 10 ml $H_2O_2$, 1 ml HF, and 1 ml $HNO_3$ in conjunction with a clean cloth wheel was used to achieve a smoother surface. Specimens were etched for 1 to 3 minutes with a solution of 100 grams molybdic acid, 150 ml water, 50 ml hydrofluoric acid to expose the grain boundaries. The extruded material had a recrystallized, equiaxed grain structure, shown in Figure 3.1, with an average linear intercept grain size of 39 $\mu$m.

### Tensile Testing

Uniaxial tensile tests were conducted to determine the monotonic BDTT for this heat of material. Blanks for cylindrical, button-head, tension specimens were electro-discharge machined from the extrusion and ground parallel to the extrusion axis. The tensile specimens had approximately 30 mm long and 3 mm diameter gage sections as shown in Figure 3.2. The gage sections were electropolished in a methanol-10% perchloric acid solution at 205 K and 1.0 Amps prior to testing to eliminate surface flaws that could results in premature failure.

Tensile specimens were tested in a screw-driven Instron test frame at a constant cross-head speed of 0.254 mm/min which corresponded to nominal strain rate of $10^{-4}$ $sec^{-1}$. Elevated temperature tensile tests were performed at 300, 600, 650, and 700 K using a resistance furnace. Two to three K-type thermocouples were beaded and tied to each tensile gage section using Ni wire. Thermal gradients along the gage section were assumed to be minimal since NiAl has high thermal conductivity (~40 W/m K from 600 to 700 K). Measured differences in thermocouple temperatures were less than 4 K.

Load versus time data for the tensile tests were recorded on a strip chart and converted to true stress, ($\sigma$), and true strain, ($\epsilon$), values by assuming constant volume during plastic deformation.

$$\sigma = \frac{P_i}{A_o} \times (1 + e) \tag{3.1}$$

$$\varepsilon = \ln(1+e) \tag{3.2}$$

Where P is load in kg, A is cross-sectional area of the gage in $mm^2$, and the subscripts *i* and *o* represent incremental and original, respectively. True strain at failure was also measured using reduction in cross-sectional area and the two strain calculations agreed well since there was little necking at the temperatures tested. The true stress-strain curves were digitized for convenient representation.

Low Cycle Fatigue Testing

Specimen blanks were electro-discharge machined parallel to the extrusion axis and ground to the final dimensions shown in Figure 3.3. The gage section was approximately 15 mm long with a 4 mm diameter. The long shanks, shown in the figure, were necessary to separate the induction-heated gage section from the water-cooled grip ends. The gage sections were electro-polished using the same procedure as outlined for the tensile specimens, except the current was approximately 0.8 Amps. Tests were conducted on a computer controlled, servo-hydraulic SATEC test frame. Specimens were subjected to fatigue loading between plastic strain limits at a constant total strain rate. LCF tests were run at plastic strain ranges of 0.005 and 0.01 at a total strain rate of $10^{-4}$ $sec^{-1}$. The button-head fatigue specimens were held in water-cooled, collar grips. Careful alignment of grips was achieved by measuring lateral and circumferential deviations with dial gages.

Strain measurements were made using a standard MTS 12.7 mm strain-gage extensometer that had been adapted for use at high temperatures. Alumina rods with flat, sharp tips were used to extend the strain-gage knife blades. Spring tension between the alumina blades and the test frame itself was used to hold the blades in place. The geometry of the set-up leads to a reversed polarity of the displacements measured. The initial spacing between the alumina tips was measured with a travelling microscope. Calibration of the lengthened extensometer was achieved by dictating a known displacement using a dial micrometer, calculating the actual strain based on the initial blade spacing, and adjusting the control unit potentiometer such that the strain calculated was associated with the corresponding analog voltage.

All analog voltages measured by the transducers for this test frame (load, displacement, and strain) were calibrated in English units. The frame controller converted these analog inputs to digital values which could be represented in up to three types of units. Conversion constants were entered into the central processing unit such that load was monitored as stress (instantaneous load divided by the specimen's original cross-sectional area and adjusted by the appropriate unit conversion constants), displacement was monitored in millimeters, and total strain was monitored as millistrain (strain multiplied by $10^{-3}$). The control unit was also responsible for continuous calculation of plastic strain, $\epsilon_p$. This was accomplished by subtracting the calculated elastic strain, $\epsilon_e$, ($\epsilon_e = \sigma/E$ where $\sigma$ is the real-time, instantaneous stress and E is the slope measured from the linear elastic response of the specimen) from the real-time, instantaneous total strain, $\epsilon_t$. For each cycle of a fatigue test, the displacement rate was being dictated by the measured total strain and

the end points for the cycle were dictated by the calculated plastic strain. During fatigue testing, data collection consisted of recording stress verses time on a strip chart, stress verses total strain on a x-y recorder, and stress verses total strain on a computer data acquisition system (SATEC's Gentest).

The test temperatures of 600, 675, and 700 K were chosen based on the monotonic test results and achieved using a 2 KW induction furnace. The induction coil was designed by trial and error to achieve uniform heating. The final coil was made of 6.35 mm, copper tubing. Three wraps were made, pancake style, to coincide with each shoulder and were connected by a straight segment parallel to the specimen gage, Figure 3.4. K-type thermocouples were beaded and melted onto the specimen surface using a spot welding technique and very low current. Repeated heating of several different specimens with as many as seven thermocouples welded to the gage and shoulders determined that a maximum temperature gradient of 10 K could be achieved in the gage section when the coil was properly centered. When using thermocouples attached only at the top and bottom shoulders to control the furnace, the average gage temperature could be maintained within $\pm$ 5 K of the desired temperature.

Microscopy

Fracture surfaces and gage section surfaces were examined in a Hitachi S-800 scanning electron microscope (SEM) with a field emission tip and a Cambridge with a tungsten filament. Transmission electron microscopy (TEM) was conducted on a JOEL 100 CX at accelerating voltages of 100 and 150 KeV. Discs for TEM foils were sliced from gage sections using a low speed saw and silicon carbide blades. Discs were mechanically ground to thicknesses of 0.18 to 0.25 mm using 400 and 600 grit paper. TEM foils were prepared by thinning discs in a solution of 70% ethanol, 13.7% water, 10% butyl cellosolve, and 6.3% perchloric acid. A Tenupole twin jet polisher was used with polishing conditions of approximately 268 K and 0.2 amps. Foils were prepared from as-extruded material to confirm that the preparation process was not introducing deformation. Burger's vector analysis was conducted using the $\mathbf{g}\cdot\mathbf{b}$ invisibility criterion. The 180° ambiguity frequently encountered in TEM analysis was avoided by generation of a stereographic projection (for the beam direction normal to the foil) for each grain analyzed.

## RESULTS AND DISCUSSION

### Tensile Testing

The true stress versus true strain data for tensile tests conducted at $\dot{e} = 10^{-4}$ $s^{-1}$ are shown in Figure 4.1 (initial strain off-set from zero for clarity). The room temperature (300 K) test failed elastically. Previous work in NiAl has shown that the fracture stress with zero ductility corresponds to the yield stress. For this heat of material tested at $10^{-4}$ $s^{-1}$, the yield stress dropped from 155 MPa at 300 K to 141 MPa at 700 K and the fracture stress increased from 155 to 374 MPa in the same temperature range. The percentage of intergranular fracture, relative to transgranular cleavage, in the fracture surfaces decreased with increasing temperature from 39 ±4% intergranular at 600 K to 28 ±2% at 700 K, Figure 4.2.

Figure 4.3 demonstrates that tensile elongation showed a precipitous increase with temperature and closely resembled previously published curves [15]. Plastic strain was calculated both from the load-time chart by assuming constant volume and by calculating the reduction in area from the diameter of the gage after failure. Good agreement was obtained from these two methods. A BDTT of 650 K was obtained from the data in Figure 4.3 using the method previously described. This is a relatively high BDTT compared to average transition temperatures for polycrystalline NiAl [14,16]. Of the factors identified in reference 16, the vacancy content resulting from the cooling rate from the extrusion is the most likely reason for the high BDTT of this heat. The composition and interstitial content of this alloy is comparable to those studied previously [16].

### Low Cycle Fatigue Testing

A single fatigue geometry specimen was tested in tension on the SATEC test frame to confirm reasonable duplication of test/temperature conditions. Table 4.1 shows the scatter in data between the two samples was no greater than one might expect for repeat test using the same equipment. Fatigue specimens were tested with $\dot{e} = 10^{-4}$ $s^{-1}$, at one temperature below the BDTT and two above, and at plastic strain ranges of 1.0% and 0.5%. Fatigue tests were conducted at 600, 675, and 700 K; temperatures which corresponded to monotonic tensile ductilities of approximately 2, 7, and 18%.

#### Fatigue Response

The change in fatigue response with temperature for both plastic strain ranges is shown in Figure 4.4. Cumulative plastic strain used as the horizontal axis in these figures is the number of cycles multiplied by the imposed plastic strain range. Figure 4.5 shows an example of the hysteresis loops, recorded intermittently on an x-y plotter, which confirmed the accuracy of the test control as well as provided the stress amplitudes as a function of number of cycles. In all test conditions, rapid hardening occurred for the first few cycles. No cyclic softening or load drop was observed under any conditions. Figure 4.6 shows the estimated fatigue life curves for 600 and 700 K using the universal slopes equation. Since there was no necking at these temperatures, fracture strength was substituted for ultimate

strength. Also shown in the previous figure are the results of this study plotted as total strain range at the end of life versus cycles. These data points are not statistically significant, but show approximate agreement with predictions.

The shape of the cyclic hardening curves (Figure 4.4) did not change significantly within this test matrix. Many of the tests which had extensive lives (greater than 100% cumulative strain) showed increased hardening toward the end of their lives. For ease of discussion, the cyclic hardening curves were divided into four regions, Figure 4.7. These region were characterized by an initial hardening region, a stress plateau, additional hardening, and a return to relative stability. Duplicate tests or interrupted tests always yielded the same cyclic hardening curves, an example of which is given in Figure 4.8 (a,b). A slight asymmetry was seen between tensile and compressive stress amplitudes under the most severe test condition, 600 K and 0.1% plastic strain range, Figure 4.9 (a). As illustrated in Figure 4.9 (b) however, most test conditions did not result in noticeable differences between the magnitude of tensile and compressive stresses measured in a given load cycle.

Fracture Surface Observations

The fracture surfaces of the fatigue tests looked surprisingly similar to those of the tensile tests, Figure 4.10 (a,b). Figure 4.10 (b) shows the internal inclusion that initiated the fracture. X-ray dispersive analysis indicated high levels of Si in the inclusions. These inclusion were non-metallic and quite likely silica which is a common crucible material used in powder production. At 600 K all fatigue fractures initiated at internal inclusions, like the one shown in Figure 4.10 (b). Above the BDTT, some failures initiated at inclusions but repeat test had longer lives and failures were initiated at the surface. Therefore at 675 and 700 K, flaw sensitivity appeared to be diminishing. There were no clear demarcations between areas of cyclic crack growth and fast fracture for any of the specimens. Studying the fracture surfaces would suggest that the critical flaw size was quite small and that fast fracture dominated much of the surface. The regions directly adjacent to the fracture initiation sites were one hundred percent transgranular cleavage, but that is also the case for tensile fracture which initiate at a macroscopic flaw. The percentage of intergranular fracture in the bulk fracture surfaces of fatigue specimens tested at $\Delta\epsilon = 0.005$, Figure 4.11, decreased with increasing test temperature from 47 $\pm$6% at 600 K to 33 $\pm$4% intergranular fracture at 700 K following the same trends seen in the monotonic failures. Note that the percentage of intergranular fracture for the fatigue test at 675 K and $\Delta\epsilon = 0.005$ was unexpectedly low, 32%, but this specimen failed at a very short life from an unusually large inclusion.

Surface Deformation Observations

The gage surfaces of fatigue samples showed evidence of deformation. Slip traces and secondary cracking were common on specimens cycled to failure. Surface slip traces occurred at all temperatures and both strain ranges on specimens which reached initial saturation. Figure 4.12 (a,b) shows an example of slip bands which developed into distinct extrusion on the surface of a specimen which failed in region IV. The samples which had lives longer than 1500 cycles showed not only the macroscopic slip bands seen in many samples, but also contained very fine lines, Figure 4.12 (b). These fine slip bands were quite

linear and uniformly spaced, and were only observed in specimens which were deformed into region IV. The concentration of slip traces was slightly higher near the fracture surface, but they were not limited to the center of the gage section. Even surfaces which had fairly sparse bands of intrusions/extrusions had bands extending to the shoulder radius, Figure 4.13 (a,b). Transgranular cracks were seen forming at some deep slip bands. In addition, intergranular cracks were seen opening between grains which contained slip traces.

Surface deformation was found to increase with the amount of imposed deformation and with decreasing test temperature. Figure 4.14 tracks the increasing deformation density for samples tested at 600 K and $\Delta\epsilon_p = 0.5\%$. The two specimens tested at 600 K and $\Delta\epsilon_p = 1.0\%$, Figure 4.15 (a,b), failed at the beginning of region II and revealed the most striking evidence of increasing deformation density. Both failures were initiated at internal inclusions; one of the specimens failed after 8 cycles and the other after 10. The surface deformation on the sample with 10 cycles 4.15(b) was noticeably more extensive than the deformation on the sample with 8 cycles 4.15(a). Three examples are included of the effect of increasing temperature on the extent of surface deformation. Figures 4.16 and 4.17 show surfaces from samples deformed at 700 K to the onset of stability (beginning of region II) at $\Delta\epsilon_p = 0.5\%$ and 1.0%, respectively. The sample tested at 600 K Figure 4.14 (b) had sparse but noticeable bands of intrusions and extrusions while the surface shown in 4.16 tested at 700 K more closely resembles a tensile test or undeformed sample. The sample shown in Figure 4.17 can be compared to 4.15(a,b) above. Although there was evidence of embryonic slip bands forming at the beginning of stability at 700 K Figure 4.17, they were noticeably less developed than either of the samples shown in 4.15 which were tested at 600 K. Figure 4.18(a,b) were both tested above the BDTT and interrupted in stage III. Although the sample tested at 675 K had 100 cycles less than that tested at 700 K, the surface deformation was more developed as a result of the lower test temperature.

Internal Deformation Observations

The as-extruded material used in this study was virtually free of dislocations. TEM analysis showed that dislocations density was high in the interior of the fatigued specimens. Burgers vector analysis was conducted on specimens which were interrupted early in life for strain amplitudes of 0.5% tested at 600 and 675 K. All the dislocations identified had <100> Burgers vectors. Dislocation morphologies observed after cyclic deformation were regions of uniformly distributed tangles, equiaxed cells, elongated cells, and dislocation veins all with walls of varying thickness. For the purpose of this discussion, the dislocation veins span the width of a grain virtually unobstructed. Elongated cells, on the other hand, had lengths less than the grain width and were usually not as well aligned as veins. The interiors of the cells and veins frequently contained dislocation loops. The morphology of the dislocation structures changed with increasing deformation and did not change as a function of temperature. The dislocation density did, however, decrease with increasing test temperature.

Observations of the dislocation structures implied that the changing morphologies corresponded to the changing shape of the cyclic hardening curves. Test specimens interrupted during the initial hardening stage of fatigue, region I, had dislocation structures which resembled those reported for interrupted monotonic deformation [16,18]. After as

little as one fully reversed cycle of $\Delta\epsilon_p$ = 0.5%, Figure 4.19 shows that a cellular structure was beginning to form. After five cycles under the same test conditions, cells with thick walls of dislocations could be readily found. The cell configurations were mixed with some cells being elongated and some being equiaxed in shape, Figure 4.20(a,b). Cellular morphologies dominated through region II of the fatigue curve. Samples which were deformed into regions III and IV had dislocation morphologies which were predominantly filled with veins of dislocation tangles. The transitions were not precise, but detailed observations suggest that the predominant structure changed with cumulative deformation. Figure 4.21 shows a typical cyclic hardening curve for a specimen deformed to failure at 600 K, $\Delta\epsilon_p$ = 0.5% and the characteristic dislocation structures from interrupted samples tested under those conditions. A similar figure is shown in Figure 4.22 for samples tested at 700 K, $\Delta\epsilon_p$ = 1.0%. It is interesting to note that grains, or large areas of grains, devoid of a well defined structure and containing uniformly distributed dislocation tangles were infrequent in tests interrupted in regions I or II but fairly common in tests to failure in regions III and IV. The dislocation structures did not appear to planar based on tilting experiments and stereo imaging.

Comparisons between specimens tested at different temperatures but the same accumulated strain show that the dislocation density decreases with increasing test temperature. This change in density makes comparisons between dislocation morphologies for the same strain difficult. The same dislocation arrangements seemed to be present at all three temperatures. At 700 K as well as 600 K samples interrupted early in the fatigue life contained mostly cellular arrays. Samples fatigued into regions III and IV (on cyclic hardening curves) had large areas of well aligned veins and areas that had been filled with tangles. Figure 4.23 illustrates the two types of microstructures seen at the end of fatigue life for both 600 and 700 K.

## Analysis of Low Cycle Fatigue Properties

The fatigue properties of polycrystalline NiAl tested between 600 and 700 K were evaluated to determine behavior trends. Comparisons were made within the test matrix, between these tests and those previously reported, and comparisons were made between these tests and predictions based on monotonic behavior. The cyclic hardening curves shown in Figure 4.4 suggested that the deformation mechanisms were not changing within this temperature range because the shape of these curves was not altered. Yet, the accumulation of damage was changing with changes in strain or temperature. The development of the surface deformation, higher density with increasing strain at a constant temperature and lower density with increasing temperature at a constant level of strain, was direct evidence of the deformation trends suggested by the cyclic hardening curves. Low cycle fatigue properties did not change abruptly within the 100 K temperature range. The change in the saturation stress, shown in Figure 4.24, associated with Region II on the cyclic hardening curves indicated a possible transition associated with the monotonic BDTT.

When compared to the previously mentioned fatigue studies, the fatigue properties of NiAl between 600 and 700 K more closely resembled the behavior at room temperature. NiAl cyclicly hardened under all the test conditions between 600 and 700 K in agreement

with low temperature results and at odds to those at 1000 K. The similitude was however not exact; the cyclic hardening curves at room temperature hardened continuously without the plateau seen near the BDTT. Also analogous to the low temperature behavior, the fracture surfaces in this temperature range showed little if any cyclic crack growth. The initiation sites were surrounded by transgranular cleavage, but these regions could not be precisely identified as ones of cyclic growth. These cleavage facets did not show typical fatigue damage and looked similar to cleavage facets found on tensile surfaces. It was interesting to note that both of the previous room temperature studies which have been reported in some depth [28,32] commented on the sensitivity of the fatigue tests to pre-existing flaws. It appeared as though, based on relative initiation sites, the fatigue tests at 600 to 700 K were more sensitivity to pre-existing flaws than the monotonic tests. There was insufficient data from this study to draw conclusions on the flaw sensitivity since the tensile and fatigue specimens were not taken randomly from the extrusion.

Conventional wisdom suggests that large increases in ductility greatly affects the fatigue life of a material in the low cycle fatigue regime. The Coffin/Manson relation predicted a two order-of-magnitude jump in cycles to failure between 600 and 700 K for samples tested at $\Delta\epsilon_p = 0.005$ using c = -0.5. The fatigue life increased by slightly more than two times within this temperature range for plastic strain ranges of 0.005, but that increase was modest compared to the prediction. The change in fatigue life was much greater for the tests conducted at $\Delta\epsilon = 0.01$, where the increase in life was two orders of magnitude. These rule-of-thumb life estimates suggested that fatigue behavior followed conventional trends at the higher but not at the lower plastic strain range. The strengths achieved at 600 K for both strain ranges, however, suggested non-conventional behavior. At both strain ranges, the stress amplitude cyclicly hardened to approximately 300 MPa at 600 K compared to tensile fracture strength of approximately 250. These figures indicate that the cyclic fracture stress exceeded the monotonic fracture stress by approximately 20%. Much less than the 60% increase measured in room temperature fatigue, but a significant trend nonetheless suggesting that a change in deformation mode is taking place from monotonic to cyclic loading.

## Analysis of Internal Deformation

Analysis of dislocation structures was necessary to ascertain what fatigue deformation was taking place that was consistent throughout this temperature range but was different than in monotonic loading. As noted in the Chapter 2, slip systems are normally the same for material deformed monotonically and cyclicly. Since <100> dislocations have dominated polycrystalline tensile and compressive deformation in all previous studies, a large presence of other dislocation types would be unexpected.

A well defined, organized dislocation structure was seen after as little as five fully reversed cycles. The similarity between this structure and those seen in interrupted monotonic tests suggest the initial deformation mechanisms are the same as one would expect. The cellular arrays did not appear to be planar based on stereo-imaging. Either cross slipping dislocations or tangling of dislocations on intersecting glide planes could have

led to this structure. This cellular structure was the only dislocation morphology seen throughout the initial hardening portion, region I, of the cyclic hardening curve.

Areas of elongated cells were noticed early in the plateau region of the cyclic hardening curve. When the lives were interrupted later in the curve, more areas of elongated cells were observed as well as regions containing distinctive veins. Region II, the stress plateau, was probably the result of cells transforming to the vein structure. Dislocations could move with less resistance within the long veins than between the cells. The dominance of the vein structure was quite evident within the samples deformed into regions III and IV. At the end of the fatigue lives, there were also more numerous and larger regions of the uniformly distributed tangles. The hardening after the plateau could indicate a significant breakdown in veins. The slightly increasing stress during the plateau region would lead to slightly decreasing vein spacing and possible collapse of the structure on a local level. The regions of uniformly distributed tangles might have resulted from collapsing veins.

The previous explanation of developing dislocation structures correlates the shape of the cyclic hardening curves with trend seen in changing dislocation morphology as a function of longer lives. The change in dislocation density is more easily understood. The initial flow stress, in both monotonic and cyclic deformation, is lower resulting in a lower number of initial dislocations. This lower initial density means a larger mean free path for subsequent deformation and, for given imposed strain, a smaller dislocation density generated per cycle. The general mobility of the dislocation is larger at the higher temperatures leading to easier cross slip and annihilation.

Small dislocation loops were evident in all the deformed TEM specimens. The density of these loops increased noticeably with the duration of the tests. A change in the number of these loops was not apparent at different test temperatures with comparable amounts of strain. Dislocation loops can occur from several sources such as accommodating precipitates or vacancies or as debris from moving dislocations.

The growth of small precipitates is often heralded by dislocations accommodating the mismatch around them. The growth of precipitates in this material is unlikely due to the good chemical stability of NiAl and the low impurity content of this particularly alloy (see Table 3.1 from Experimental Procedures). Dislocation loops also form around voids or small clusters of vacancies. NiAl has been shown to retain a large number of quenched-in vacancies [35] and these vacancies can effect material properties [16,36]. However, these vacancy loops were not created by the heat treatment associated with testing alone as shown by TEM analysis of a specimen which was held at test temperature but not deformed.

The loops could be the result of the motion of dislocations containing superjogs. This type of loop formation was used to explain debris seen in <100> single crystals [9]. Johnston and Gilman [37] and Tetelman [38] have described dislocation movement which would result in the generation of dislocation loops from superjogs either by a cross-slip mechanisms or partial annihilation of dislocation on parallel planes. Either type of loop production would explain the extreme regular spacing of loops in some areas, Figure 4.25 and correlates with the presence of long, bowing dislocations and the presence of elongated loops.

## SUMMARY

Changes were observed in the low cycle fatigue properties of near stoichiometric NiAl in the same temperature range as the monotonic BDTT, but the transition in fatigue properties was not as abrupt. In the intermediate temperature ranges tested in this research program, NiAl fatigue deformation behavior more closely resembled that of room temperature than 1000 K tests, but exhibited some differences. From 600 to 700 K fatigue specimens exhibited hardening reminiscent of low temperature behavior and had fracture surfaces that were dominated by fast fracture. The decrease in fatigue strength with increasing temperature showed a gradual transition to the characteristic high temperature softening. The small change in fatigue life over most of the test matrix and significant increase in fatigue fracture strength over the monotonic fracture strength both indicated that the deformation mechanism controlling life was changing between monotonic and cyclic.

The dislocation morphologies described previously, in conjunction with the shape of the cyclic hardening curve, suggest the following evolution of fatigue deformation substructures. During the period of initial hardening, a uniform cell structure developed. Throughout the stress plateau, the cells become elongated until a well defined structure of parallel veins forms. If the spacing between the veins becomes too small, stress interactions can cause the veins to collapse. The hardening towards the end of fatigue life is possibly associated with the break down of the metastable order created during the stress plateau. The lower density of dislocations in specimens tested at higher temperatures is consistent with the lower stress levels measured. Since the deformation mechanisms remain the same from 600 to 700 K, the increase in fatigue life should only result from the diminished rate of damage accumulation associated with the decrease in strength.

Much has been learned about the fatigue properties of NiAl in the past two years. Initial comparisons between the fatigue properties of NiAl and other B2 intermetallics [30] and superalloys [26] have been encouraging. The extremely small region of cyclic crack growth (essentially non-existent at the temperatures between 600 and 700 K) is cause for concern. However, intermediate temperature properties follow conventional trends. Further research is necessary to obtain a complete representation of fatigue deformation for NiAl.

Subsequent studies at intermediate temperature such as those probed in this project should included further TEM work. Since it is now known that the properties to not change radically in this temperature range, one test condition could be used for an in depth study of the fatigue mechanisms. Interrupted tests need to be taken at several points during region II and the transition between regions II, III and IV need further probing. Larger quantities of TEM foils could be examined for these interrupted tests to obtain exact percentages of dislocation structures at different interrupted lives.

Significantly more information is needed on internal deformation structures from LCF at all temperatures. Comparisons between dislocation activity in near surface and interior regions would be informative. Such comparisons are important since macroscopic fatigue damage lead to crack initiation on the surface. These types of experiments are, however, far from trivial to perform, as expounded upon by Keller, et al. [24].

Additional testing as a function of temperature should be conducted to look for the transition from nominally stable behavior to the profuse softening which occurs at 1000 K.

Of course the issues of creep/fatigue interaction and the effects of oxidation become important at the higher temperatures. The need for materials with ever increasing use temperatures will always exist. The NiAl system, monolithic or composite, continues to promise but there are many exciting issues remaining to be explored.

## References


1. R.D. Noebe, R.R. Bowman, and M.V. Nathal, Inter Mater. Review.
2. A.J. Bradley and A. Taylor, Proc. R. Soc., **A159**, 56-72, 1937.
3. R. Darolia, J. Metals, **43**(3), 44-49, 1991.
4. R.E. Tressler, J.R. Hellmann, and H.T. Hahn, annual report for contract NAGW-1381, Center for Advanced Materials, The Pennsylvania State University, University Park, PA, 63-65, 1990.
5. N. Rusović and H. Warlimont, phys. stat. sol., **44a**, 609-619, 1977.
6. W.A. Rachinger and A.H. Cottrell, Acta Metall., **4**, 109-113, 1956.
7. A. Ball and R.E. Smallman, Acta Metall., **14**, 1517-1526, 1966.
8. M.H. Loretto and R.J. Wasilewski, Phil. Mag., **23**, 1311, 1971.
9. R.D. Field, D.F. Lahrman, and R. Darolia, Acta Metall. Mater., **39**, 2951-2959, 1991.
10. G.W. Groves and A. Kelly, Phil. Mag., **8s.8**, 877-887, 1963.
11. A. Ball and R.E. Smallman, Acta Metall., **14**, 1349-1355 1966.
12. H.L. Fraser, M.H. Loretto, and R.E. Smallman, Phil. Mag., **28**, 667-677 1973.
13. R.D. Noebe et. al., *HITEMP Review-1990*, NASA CP-10051, 20-1 1990.
14. R.D. Noebe et. al., in *High Temperature Ordered Intermetallic Alloys IV* (Mater. Res. Soc. Proc. **213**, Pittsburgh, PA, 1991), 589-596.
15. R.D. Noebe, C.L. Cullers, and R.R. Bowman, J. Mater. Res., **7**, 605-612, 1992.
16. R.R. Bowman et al., Met. Trans., **23A**, 1493-1508, 1992.
17. G.W. Groves and A. Kelly, "Change of Shape due to Dislocation Climb", Phil. Mag., **19**, 977-986, 1969.
18. P. Nagpal and I. Baker, J. Mater. Sci. Let., **11**, 1209-1210, 1992.
19. G.E. Dieter, *Mechanical Metallurgy*, 2nd ed. (McGraw-Hill Inc., New York, 1976).
20. J.A. Bannantine, J.J. Comer, J.L. Handrock, *Fundamentals of Metal Fatigue Analysis*, (Prentice Hall, Englewood Cliffs, NJ, 1990), 52.
21. G.E. Dieter, *Mechanical Metallurgy*, 2nd ed. (McGraw-Hill, Inc., New York, 1976) 414.
22. C.E. Feltner and C. Laird, Acta Metall., **15**, 1621-1632, 1967.

23. P. Lukáš, L. Kunz, and J. Krejčí, Scripta Metall. Mater., **26**, 1511-1516 1992.

24. H.J. Roven and E. Nes, Acta Metall. Meter., **39**, 1719-1733, 1991.

25. R.R. Keller, W. Zielinski, and W.W. Gerberich, Scripta Metall. Mater., **26**, 1523-1528, 1992.

26. H. Mughrabi, Scripta Metall. Mater., **26**, 1499-1504, 1992.

27. T.L. Lin et al., Mater. Sci. Eng., **86**, 19-27, 1987.

28. K. R. Bain, R. D. Field, and D. F. Lahrman, presented at the 1991 Fall TMS Meeting, Cincinnati, OH 1991 (unpublished).

29. K.R. Bain, private communication, October 1992.

30. S. E. Hartfield-Wünsch and R. Gibala, in *High Temperature Ordered Intermetallic Alloys IV* (Mater. Res. Soc. Proc. **213**, Pittsburgh, PA, 1991), 575-580.

31. S. E. Hartfield-Wünsch, Ph.D. thesis, Univ. of Michigan, 106-116, 1991.

32. R.D. Noebe and B.A. Lerch, Scripta Metall. Mater., **27**, 1161-1166, 1992.

33. B.A. Lerch and R.D. Noebe, in *HITEMP Review 1992*, (NASA CP-10104, 1992) 47-1.

34. T.R. Smith, et al., Scripta Metall. Mater., **27**, 1389-1393, 1992.

35. H.L. Fraser, Philos. Mag., **32**, 873-875, 1975.

36. N. Rusović and E.Th. Henig, Phys. Stat. Sol., **57A**, 529-540, 1980.

37. W.G. Johnston and J.J. Gilman, J. Appl. Phys., **31**(4), 632-634, 1960.

38. A.S. Tetelman, Acta Metall., **10**, 813-820, 1962.

# TABLES

| Ni* | Al* | C | $O_2$ | S | $N_2$ |
|---|---|---|---|---|---|
| 50.48 | 49.46 | 0.014 | 0.02 | <0.003 | <0.001 |

**Table 3.1** - Composition (atomic percent)
*determined by wet chemical analysis, ±0.2 atomic percent within a 95% confidence interval

| specimen geometry | yield strength (MPa) | fracture strength (MPa) | plastic strain to failure |
|---|---|---|---|
| tensile | 148 | 246 | 0.018 |
| fatigue | 145 | 250 | 0.019 |

**Table 4.1** - Comparison between properties from samples of two specimen geometries tested in monotonic tension at 600 K and $\dot{e} = 10^{-4}$ $s^{-1}$.

| test temperature | $\sigma_f$ (MPa) | $\epsilon_f$ | n |
|---|---|---|---|
| 600 K | 246.2 | 0.018 | 0.23 |
| 700 K | 373.3 | 0.182 | 0.22 |

**Table 4.2** - Tensile test data used for simplistic predictions of fatigue response. Since necking did not occur at these temperatures, the fracture strength was taken to be the ultimate strength. Monotonic strain hardening exponent, n, was the slope of log $\sigma$ versus log $\epsilon_p$.

# FIGURES

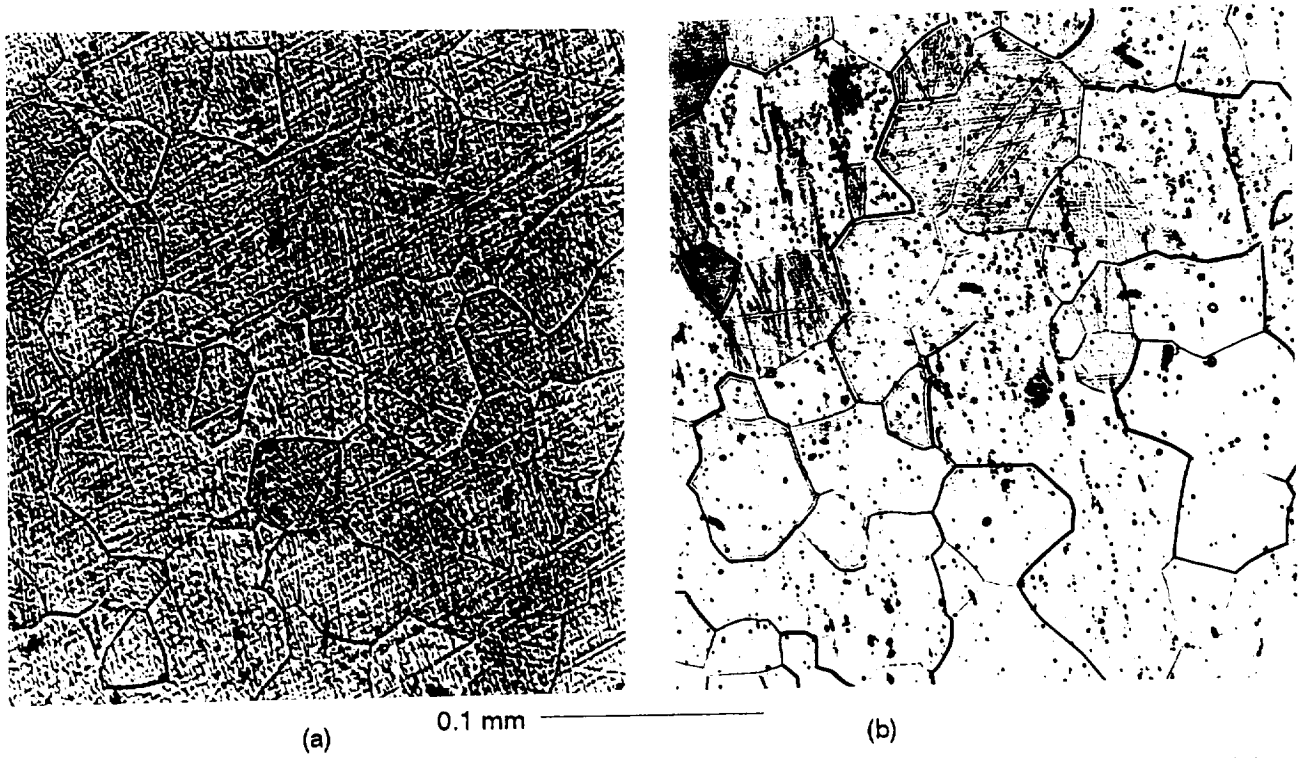


**Figure 3.1** - Recrystallized, equiaxed structure of as-extruded NiAl in (a) transverse and (b) longitudinal directions. Average linear intercept grain size is 39 $\mu$m.

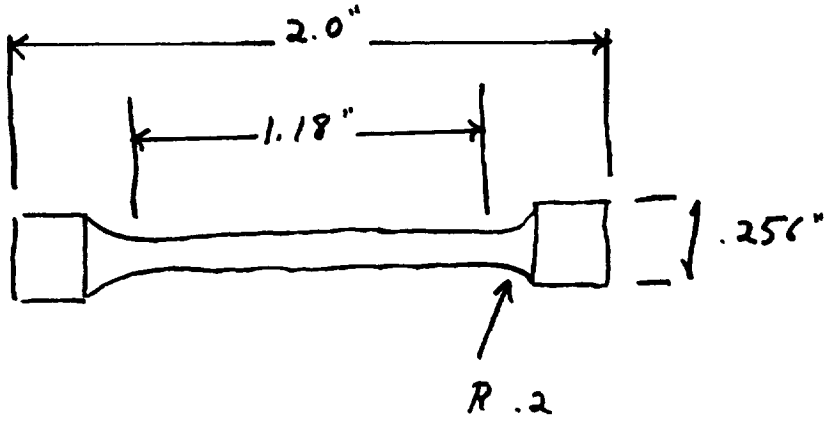


**Figure 3.2** - Specifications for tensile specimen.

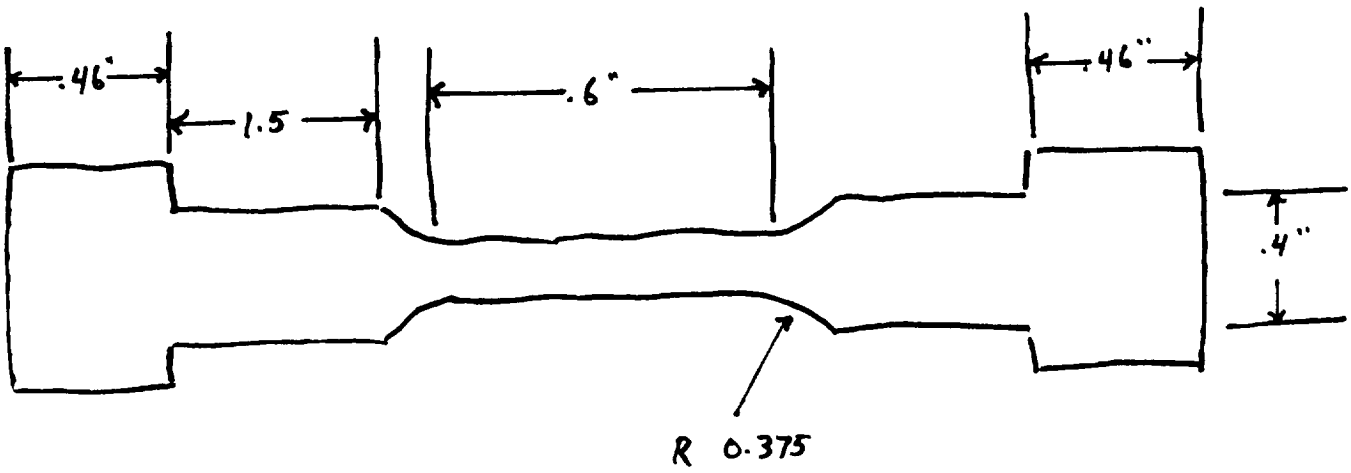


**Figure 3.3** - Specifications for low cycle fatigue specimen.


**Figure 3.4** - Induction coil design (a) front and (b) top views.

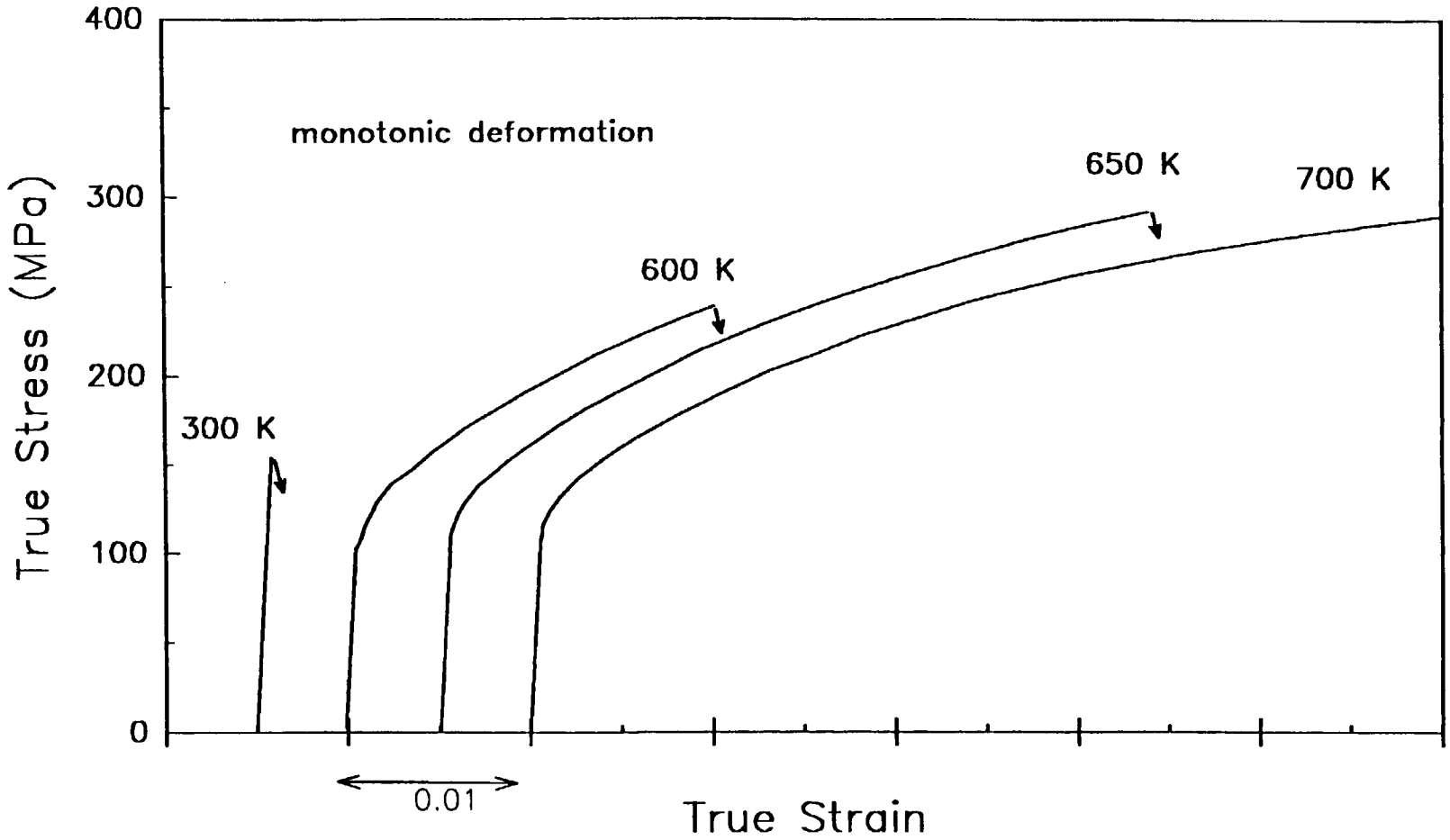


**Figure 4.1 -** True stress versus true strain for tensile test conducted at $\dot{e} = 10^{-4}\ s^{-1}$. Curves were shifted to the right for clarity. Test at 700 K continued to 18.2%.

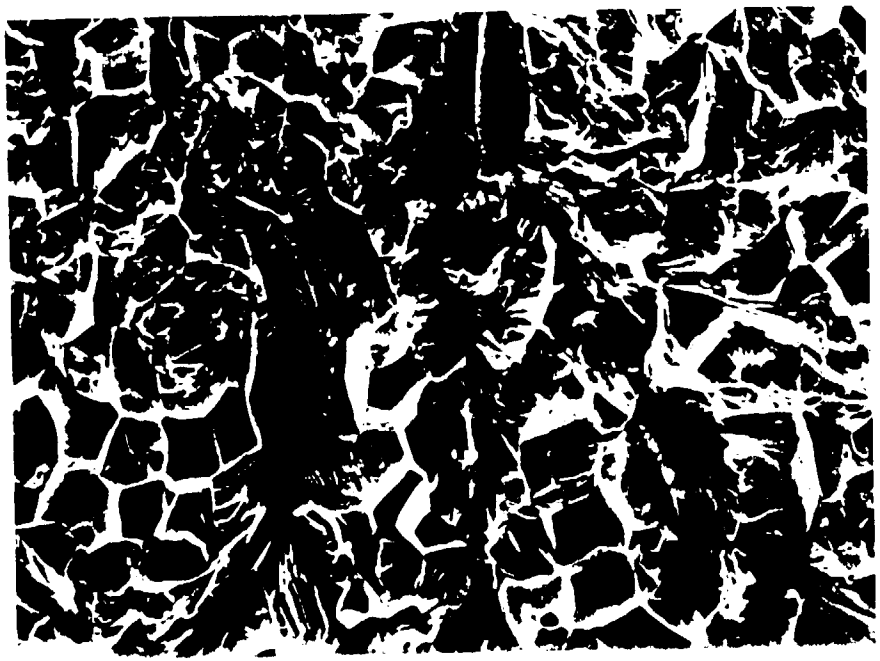

100 $\mu$m

Figure 4.2 — Portion of the tensile fracture surfaces at 700 K showing 28% intergranular fracture. Fracture initiation sites were uncertain for the tensile tests but occurred within the gage section.

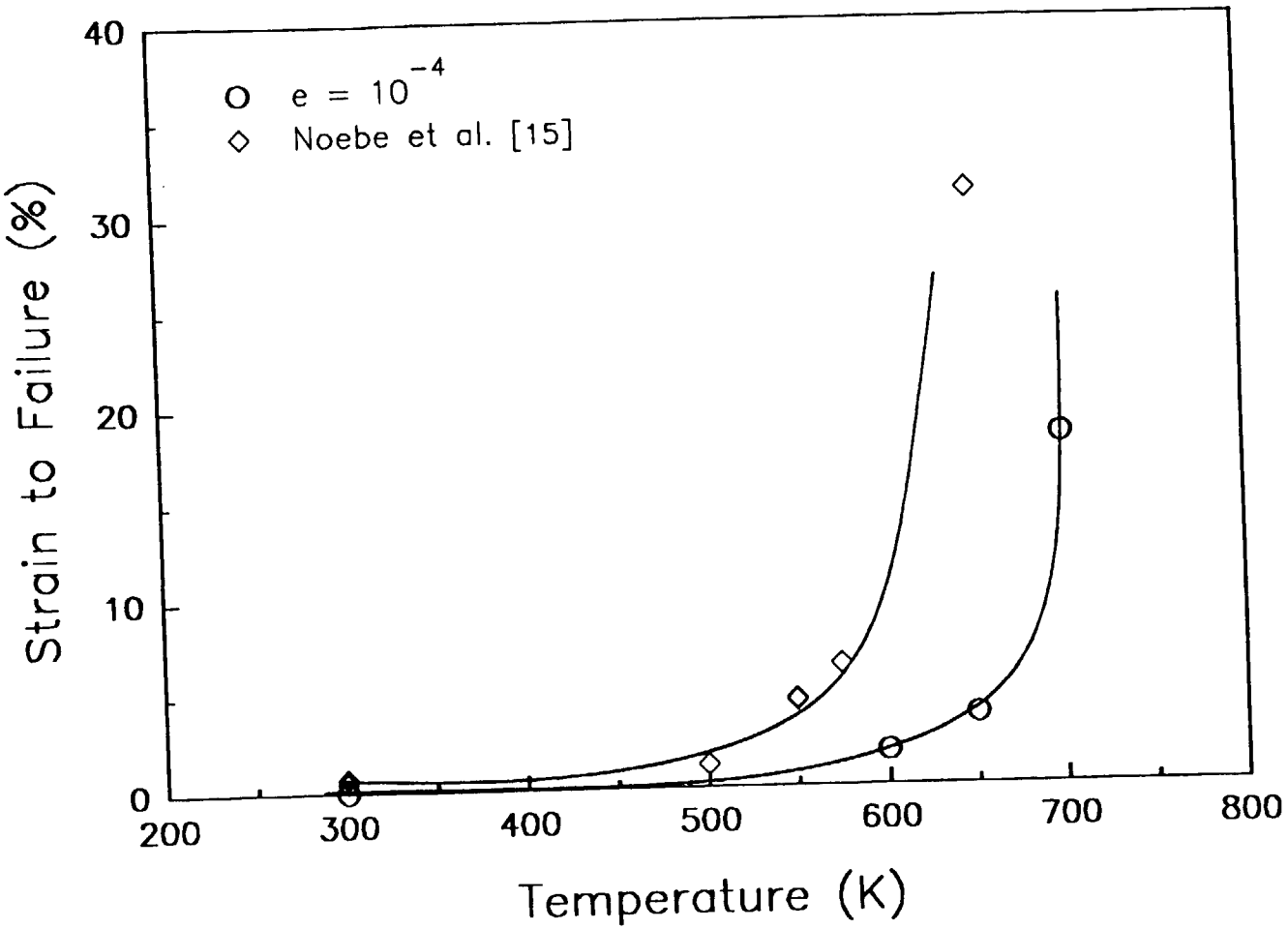


**Figure 4.3 -** Tensile true strain to failure as a function of temperature for specimens tested in this study and reported by Noebe, et al. [15] both at $\dot{e} = 10^{-4}$.

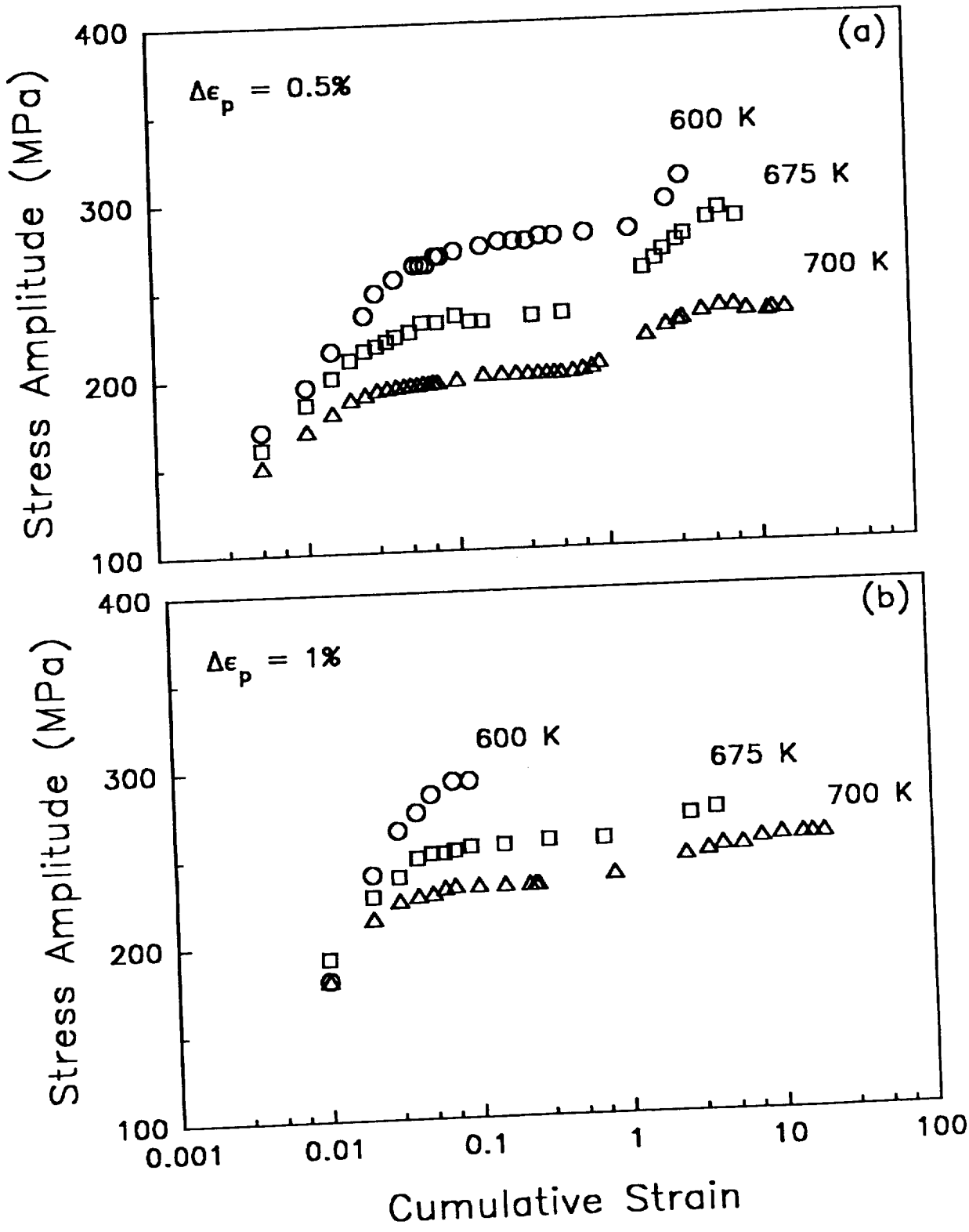


**Figure 4.4 -** Stress amplitude versus cumulative plastic strain for all three temperatures at $\dot{e} = 10^{-4}\ s^{-1}$ (a) $\Delta\epsilon_p = 0.005$ and (b) $\Delta\epsilon_p = 0.01$.

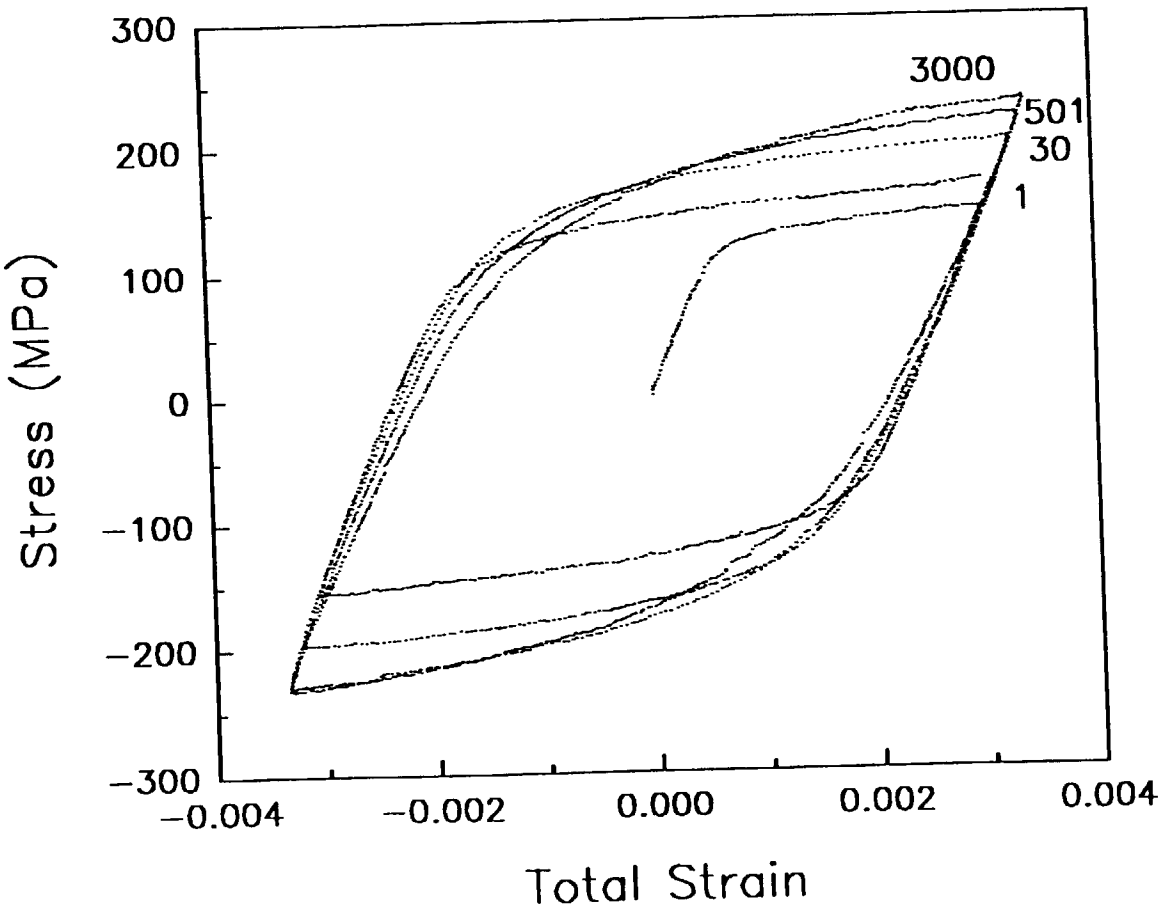


**Figure 4.5 -** Digitized points from hysteresis loops taken during a test at 700 K, $\Delta e_p = 0.005$.

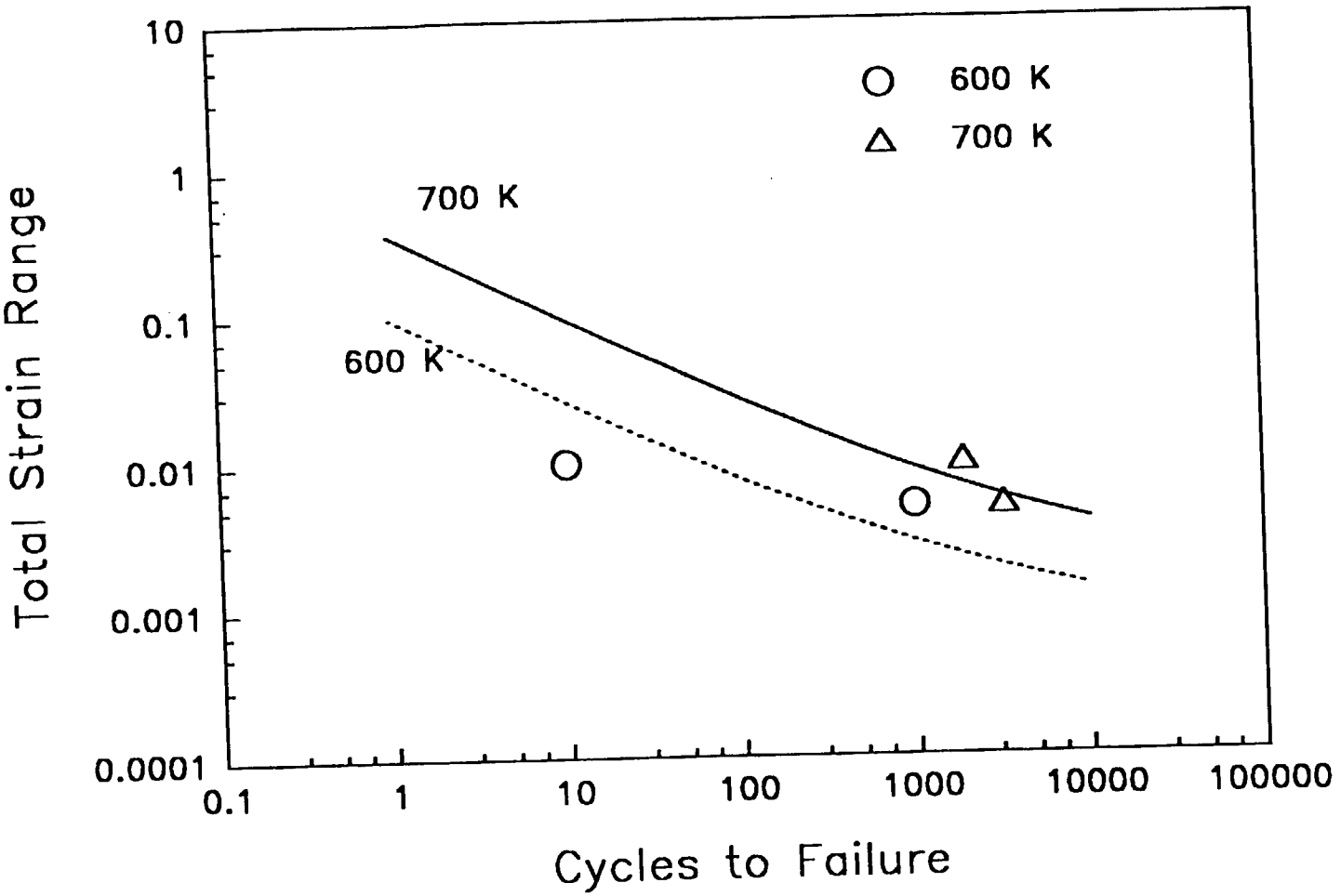


**Figure 4.6 -** Lines represent estimated fatigue lives using the universal slopes equation. Data points are total strain range at time of failure from this study.

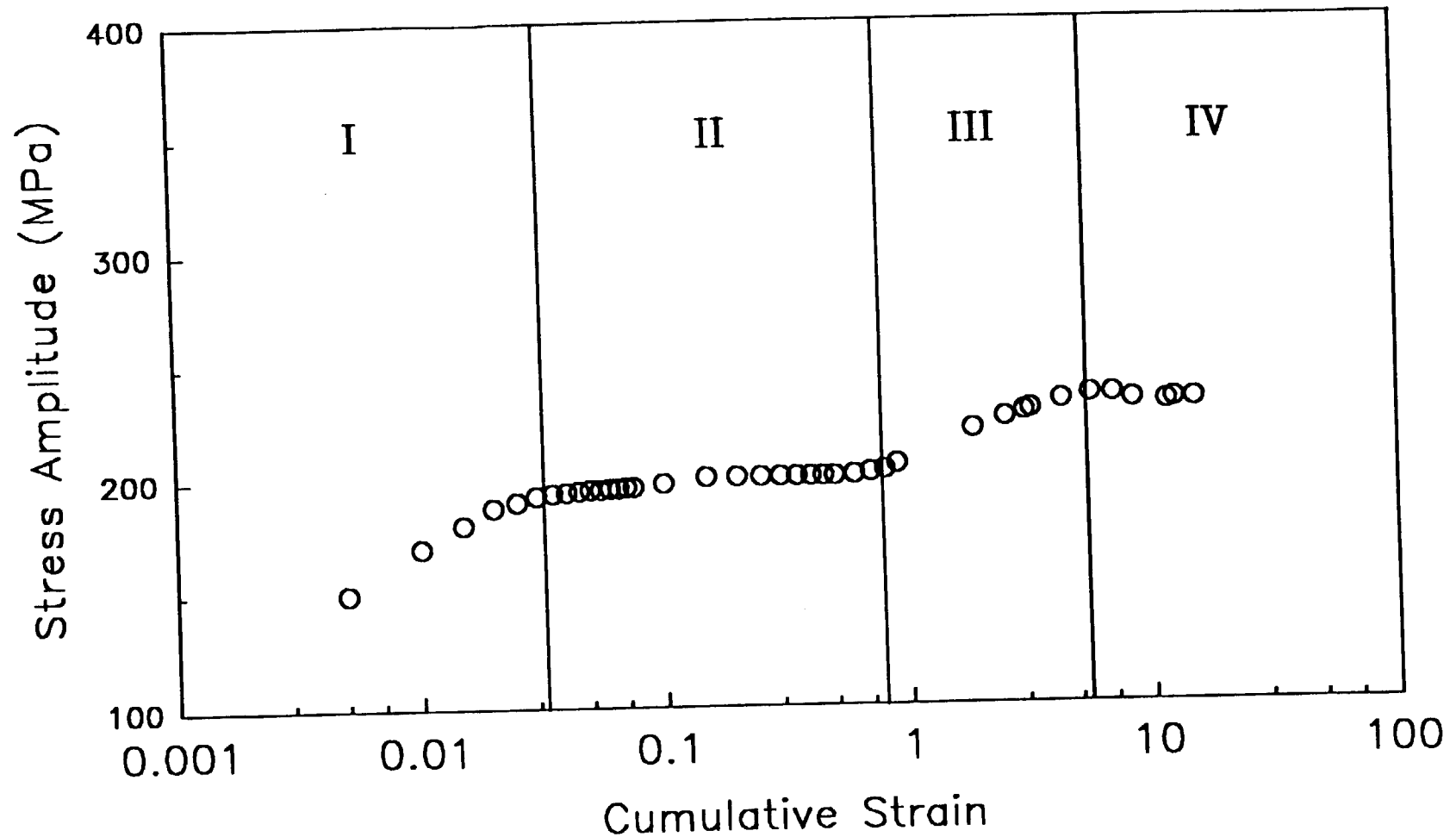


**Figure 4.7 -** Stress amplitude versus cumulative plastic strain for sample tested at 700 K, $\Delta e_p = 0.005$, and $\dot{e} = 10^{-4}\ s^{-1}$. Regions I-IV indicate areas of rapid cyclic hardening, a stress plateau, additional hardening, and returning to relative stability.

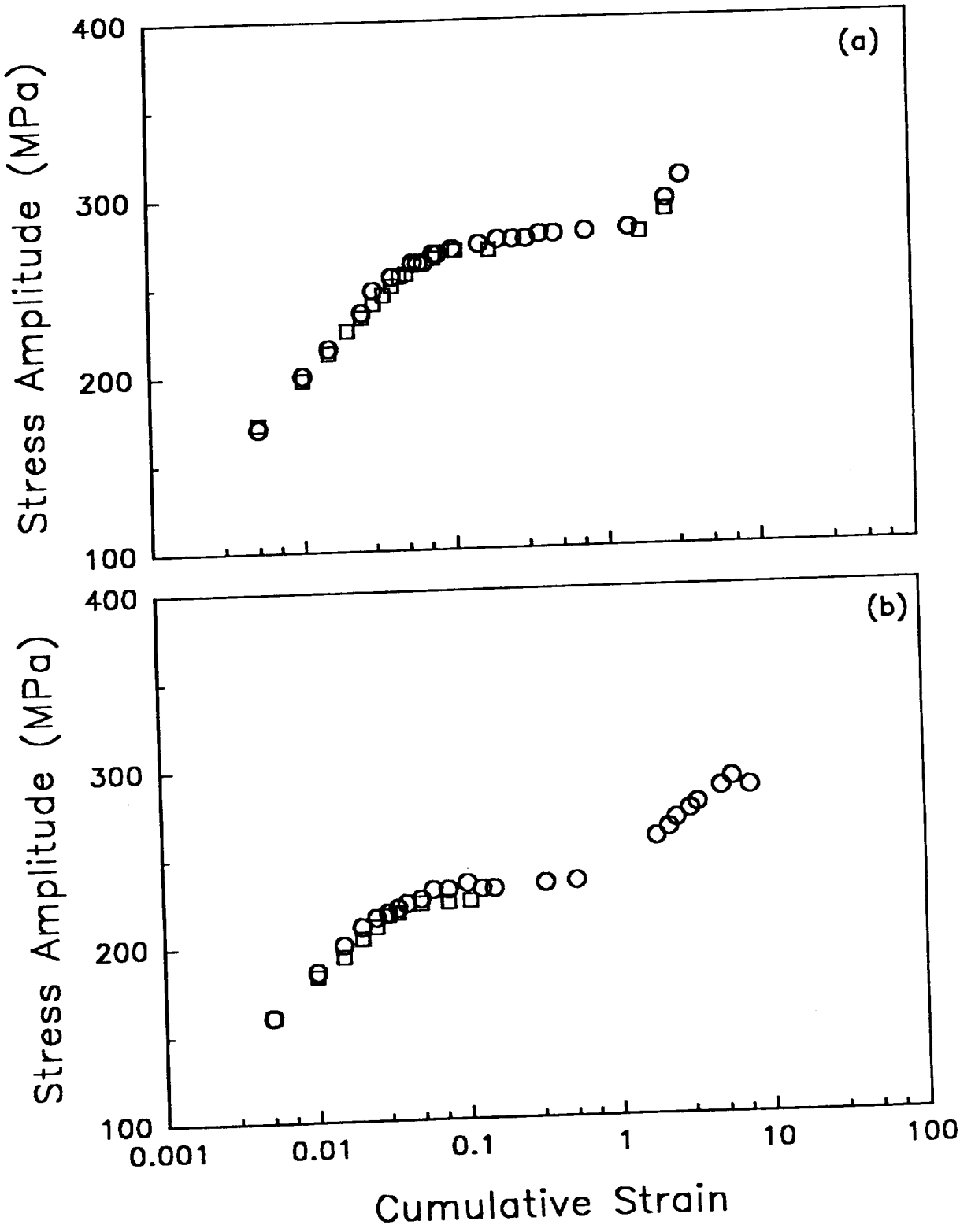


**Figure 4.8 -** (a) Duplicate LCF tests conducted at 600 K, $\Delta\epsilon_p = 0.005$. (b) Interrupted tests conducted at 675 K, $\Delta\epsilon_p = 0.01$.

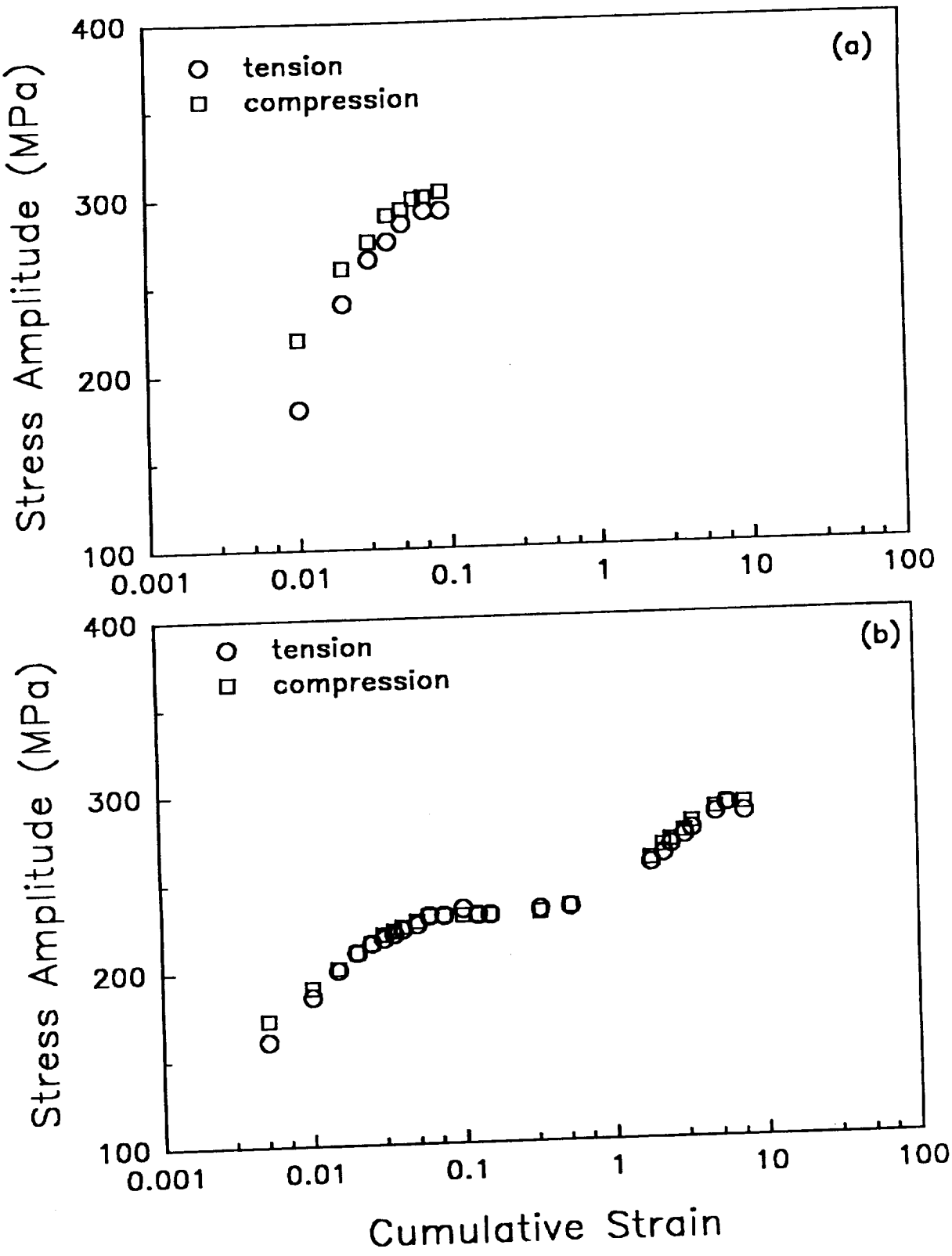


**Figure 4.9 -** Tensile and compressive stress amplitude versus cumulative plastic strain for $\Delta\epsilon_p = 0.01$, $\dot{e} = 10^{-4}\ s^{-1}$, (a) 600 K and (b) 700 K.

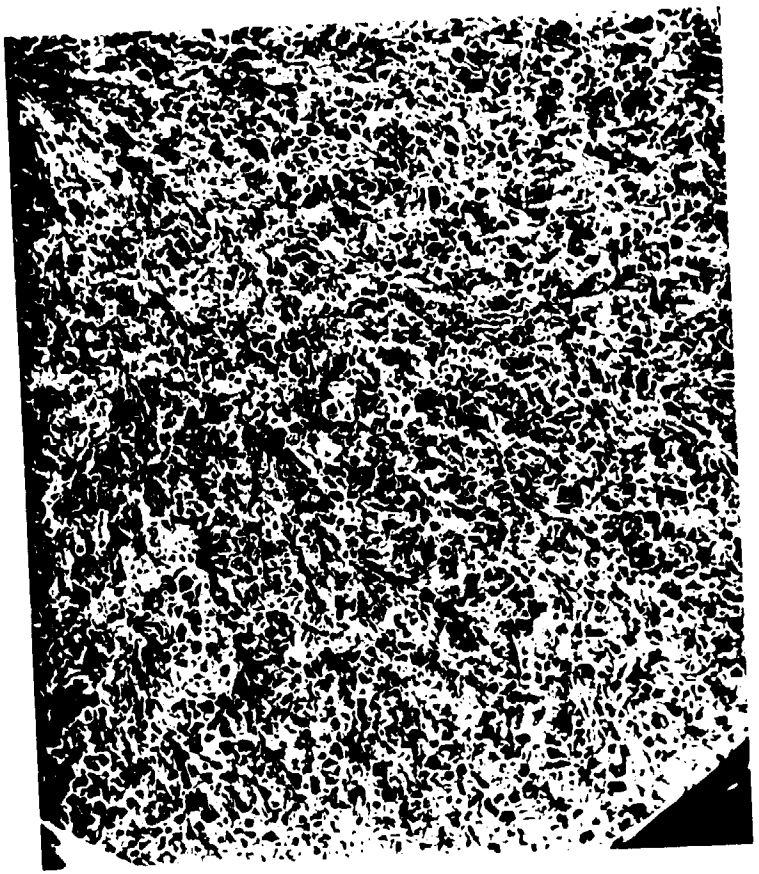

1 mm (a)

10 $\mu$m (b)

**Figure 4.10 -** Fracture surface of sample tested at 700 K, $\Delta\varepsilon_p = 0.01$ (a) low magnification with inclusion at upper left (b) inclusion. EDX analysis showed high amounts of Al, measurable amounts of Si and virtually no Ni present in the inclusion.

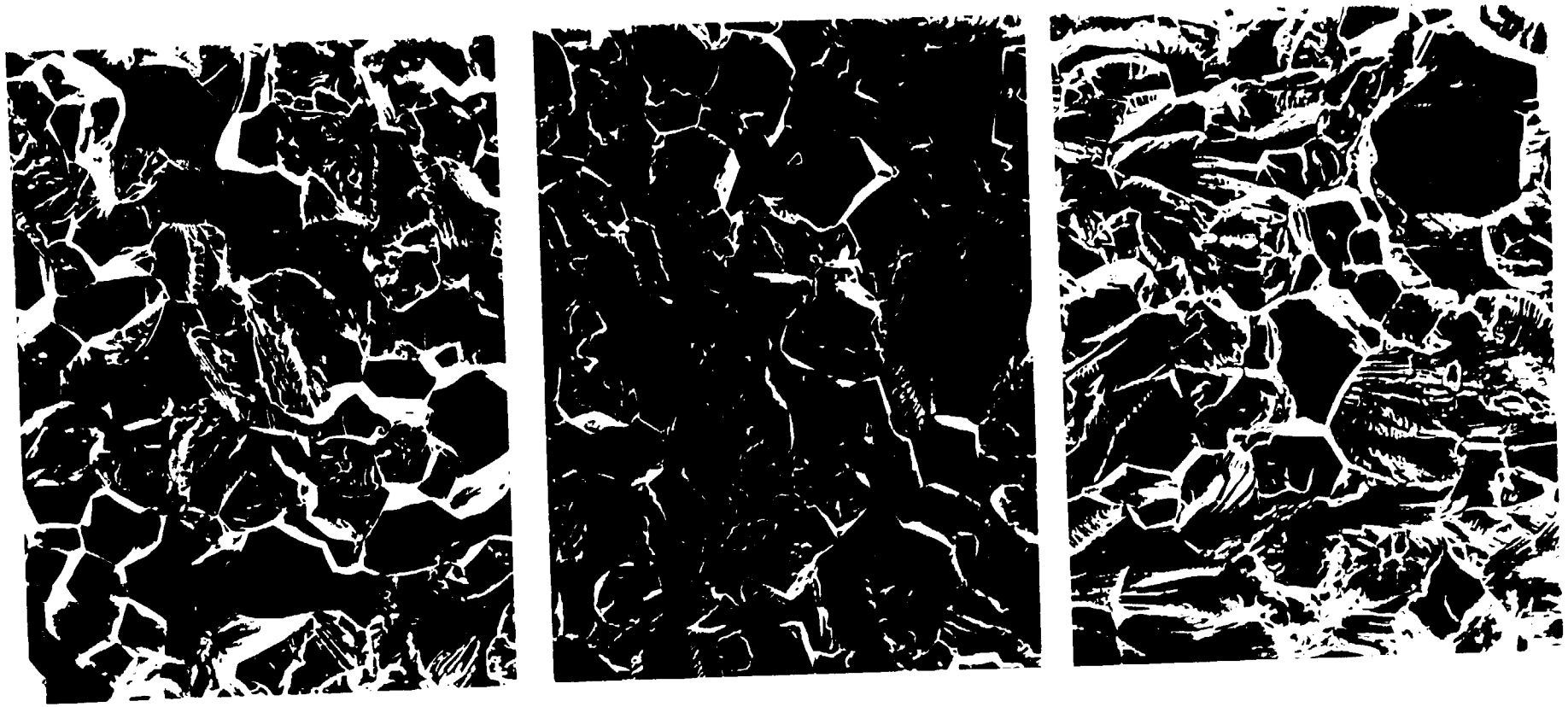


**Figure 4.11** - Portion of the fracture surfaces at (a) 600 K (b) 675 K and (c) 700 K showing, respectively, 47%, 32%, and 33% intergranular fracture.


**Figure 4.12 -** Gage surface of sample tested to failure (region IV) at 700 K, $\Delta\varepsilon_p = 0.005$ showing (a) extensive slip traces and (b) distinct extrusions and fine slip lines.

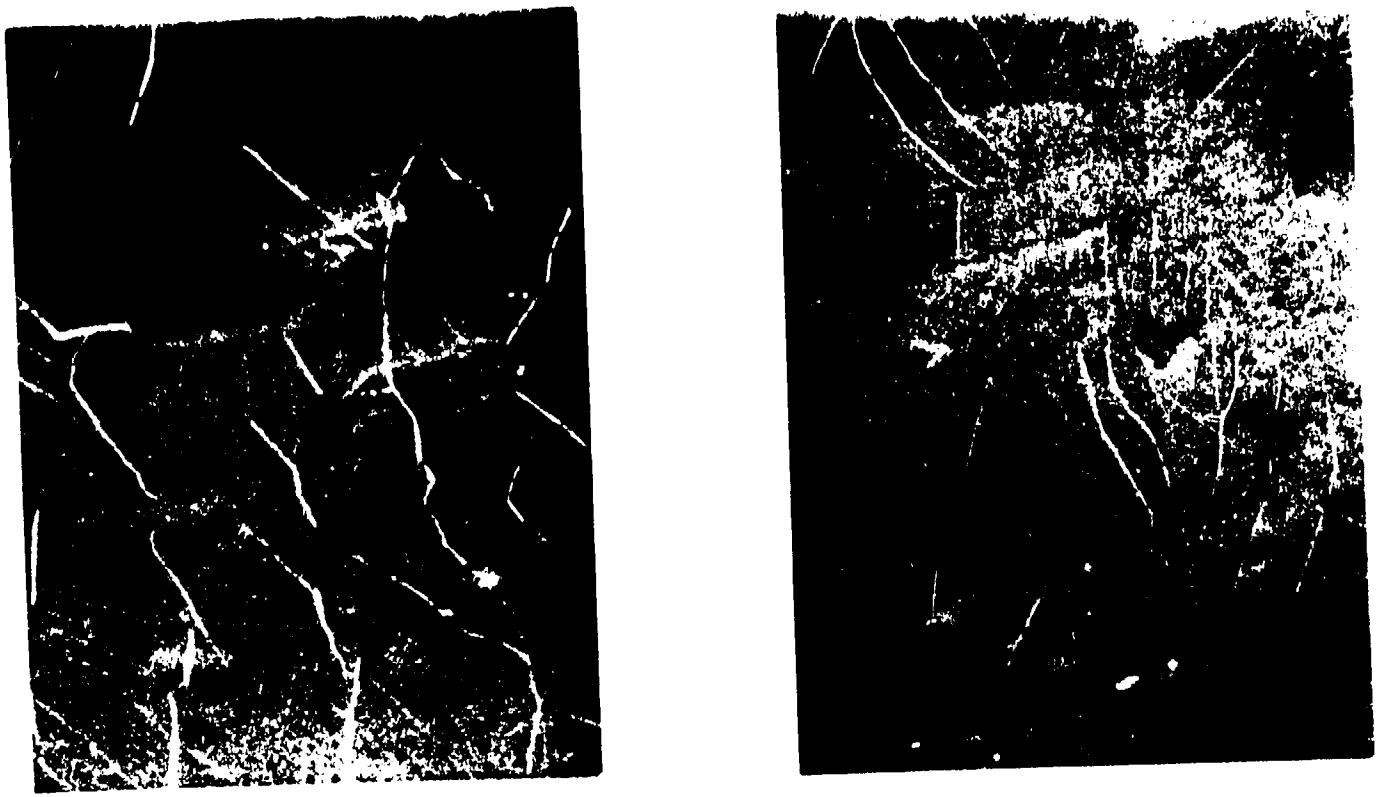


**Figure 4.13 -** Gage surface of sample tested to failure at 600 K, $\Delta\varepsilon_p = 0.01$ showing regions of slip traces (a) near the fracture surface and (b) near the radius

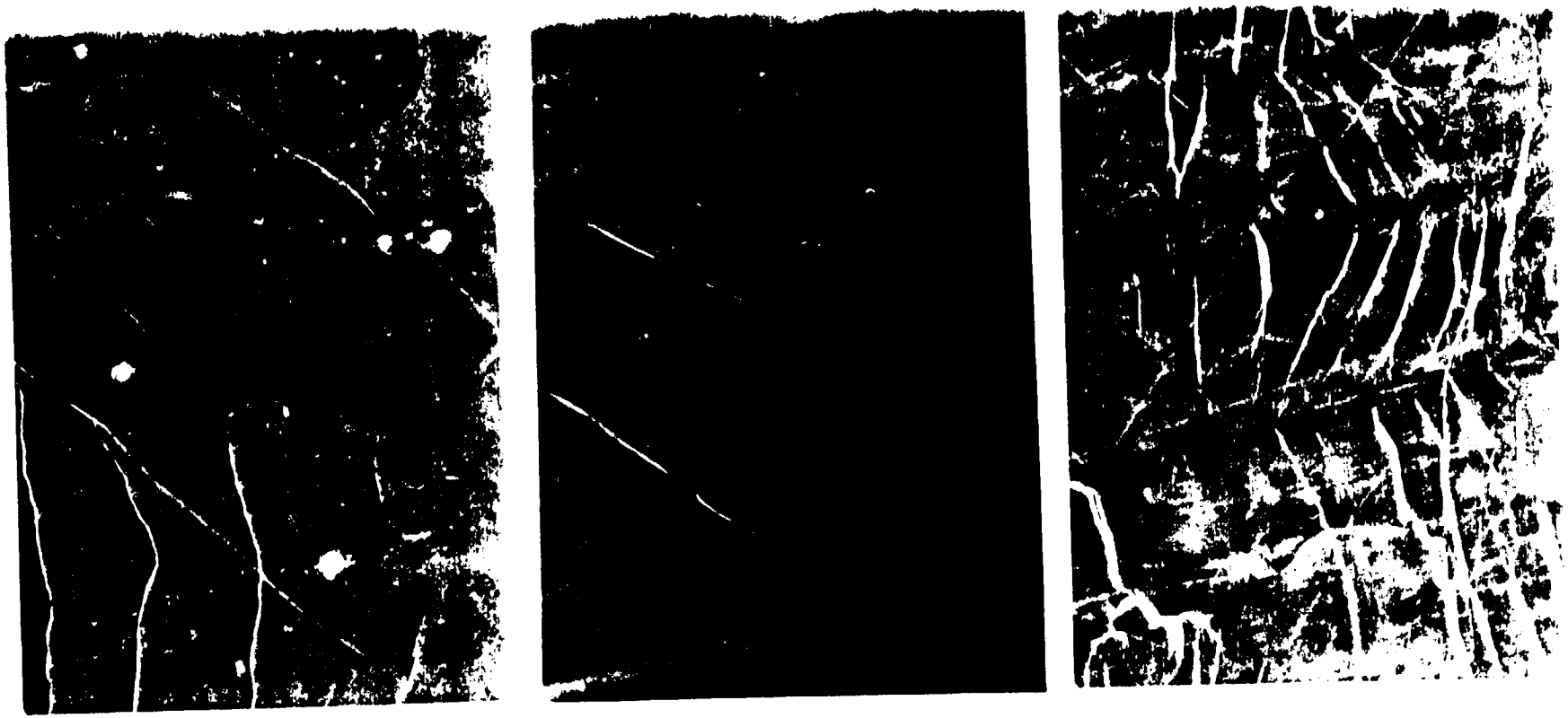


**Figure 4.14 -** Specimens deformed at 600 K and $\Delta\epsilon_t = 0.005$ (a) interrupted in region I, i.e. while cyclicly hardening, (b) interrupted in the beginning of region II, i.e. at the onset of stability, (c) failed in region III.

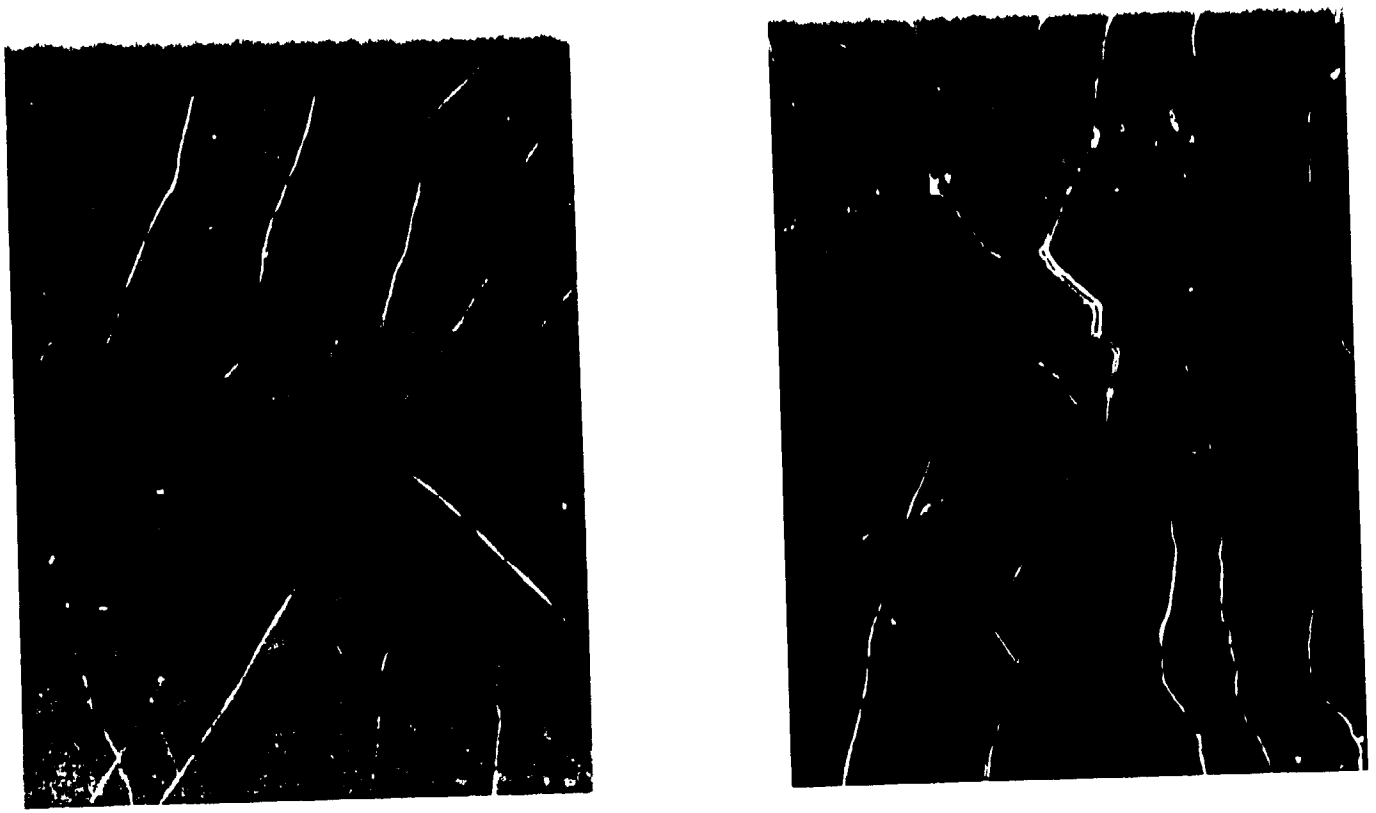


**Figure 4.15** - Specimens deformed at 600 K and $\Delta e_t = 0.01$ both failed at the beginning of region II as the result of internal inclusions (a) $N_f = 8$ and (b) $N_f = 10$.


**Figure 4.16** - Specimens deformed $\Delta\epsilon_p = 0.005$ and interrupted at the beginning of region II. 700 K. Compare to 14(b).

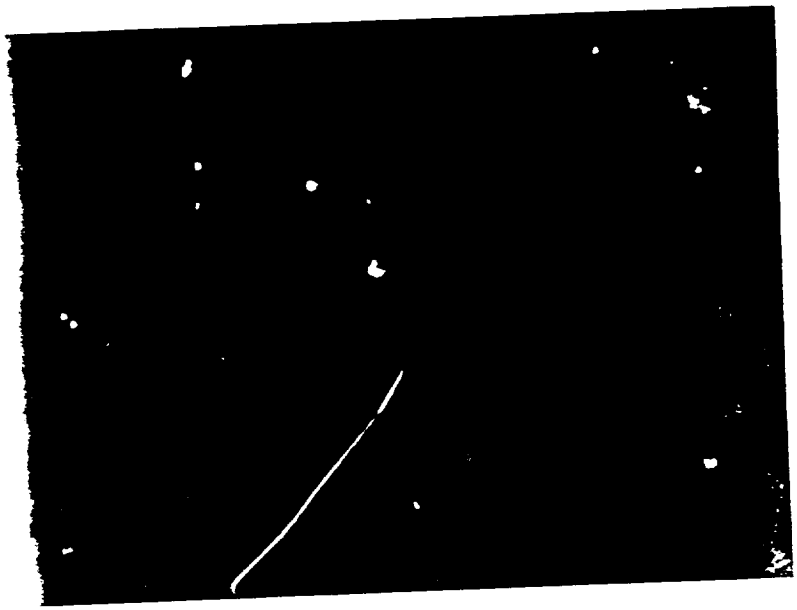


**Figure 4.17** - Specimen deformed at 700 K and $\Delta\epsilon_p = 0.01$ compare to 4.15(a,b) above.

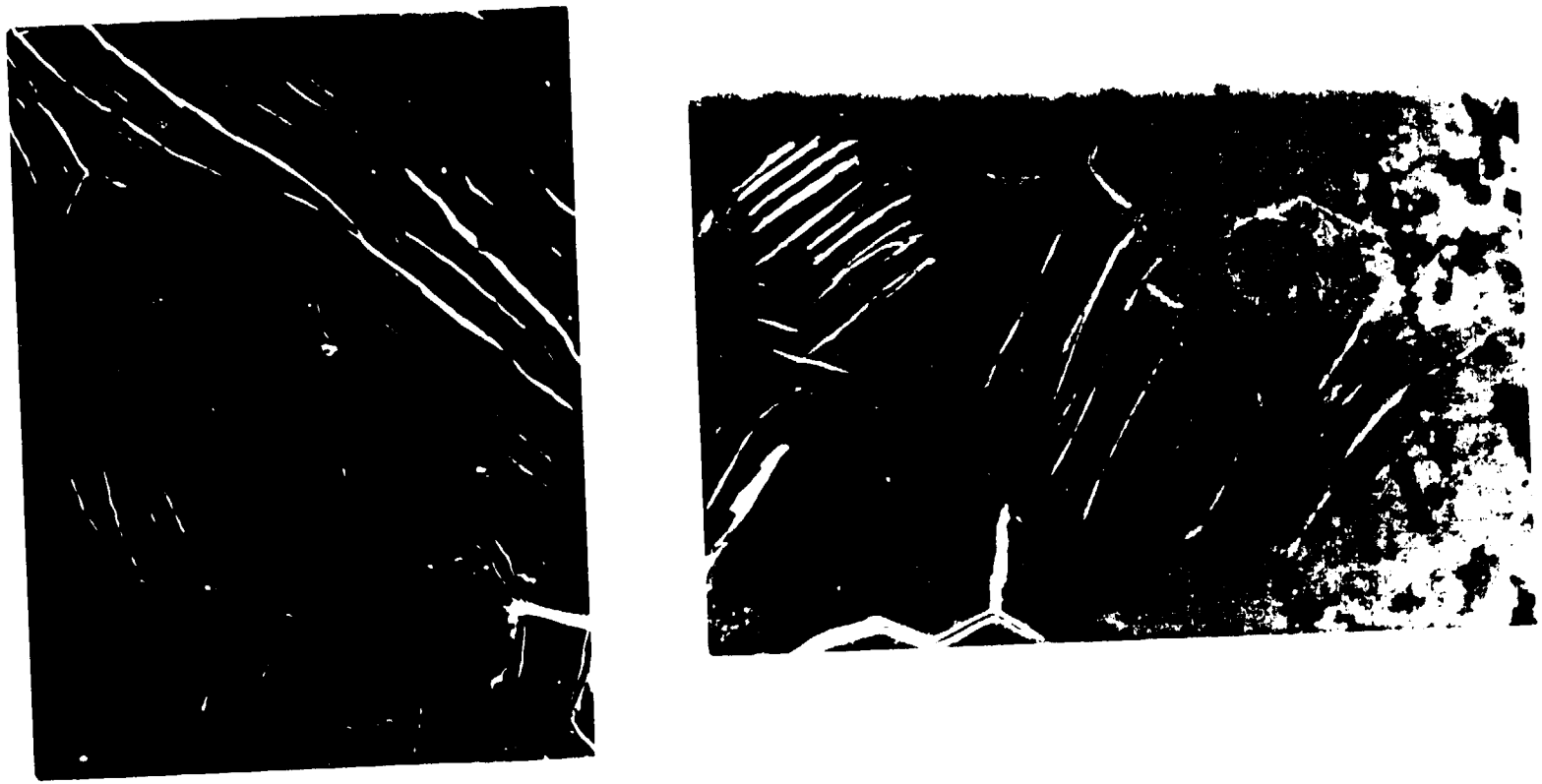


**Figure 4.18** - Specimens deformed $\Delta\epsilon_p = 0.01$ (a) 675 K and (b) 700 K. Both failed in region III as the result of inclusions. The intrusions/extrusions were more developed in (a) as the result of the lower test temperature even though specimen (a) failed 100 cycles before specimen (b).


**Figure 4.19 -** Cellular dislocation structure beginning to form after one fully reversed cycle at 600 K and $\Delta \epsilon_p = 0.005$.

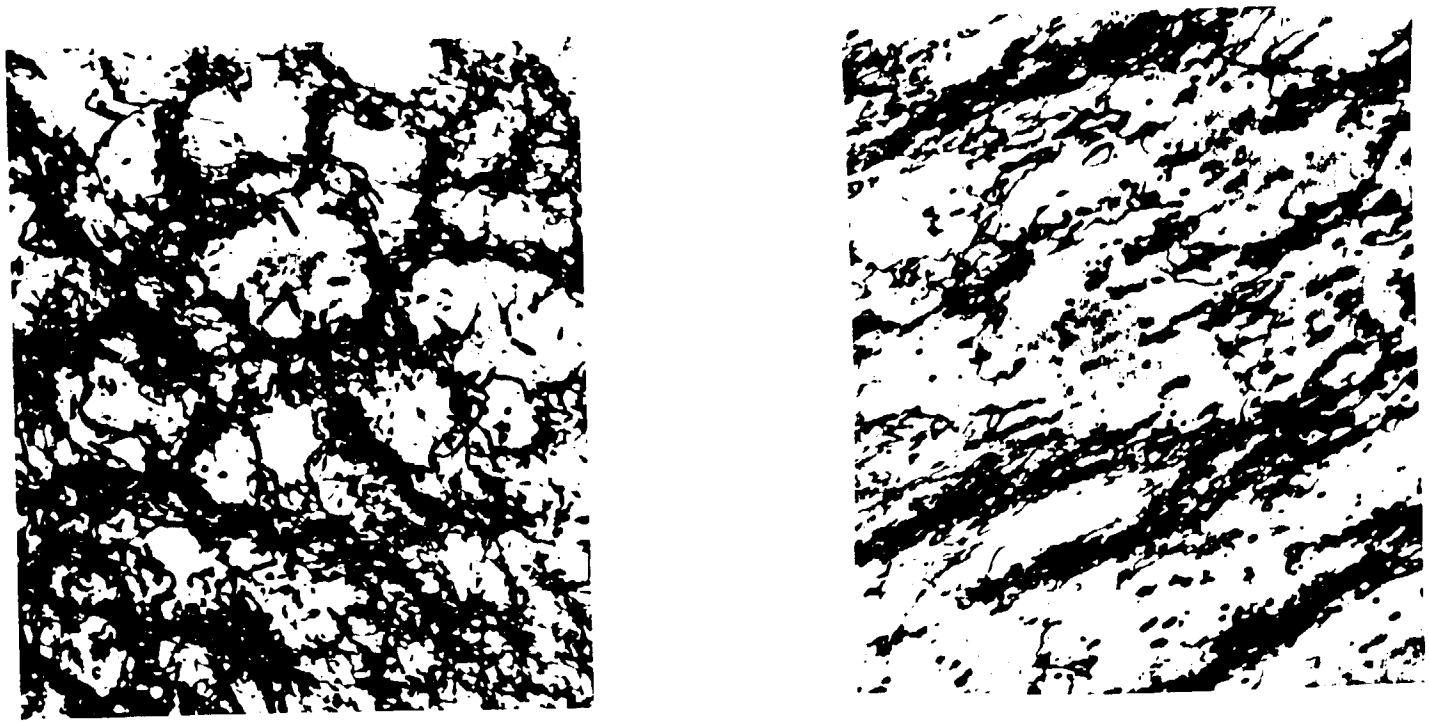


**Figure 4.20** - Well developed cells with thick walls of dislocations after 5 cycles at 600 K and $\Delta\epsilon_p = 0.005$ with (a) equiax and (b) slightly elongated configurations.

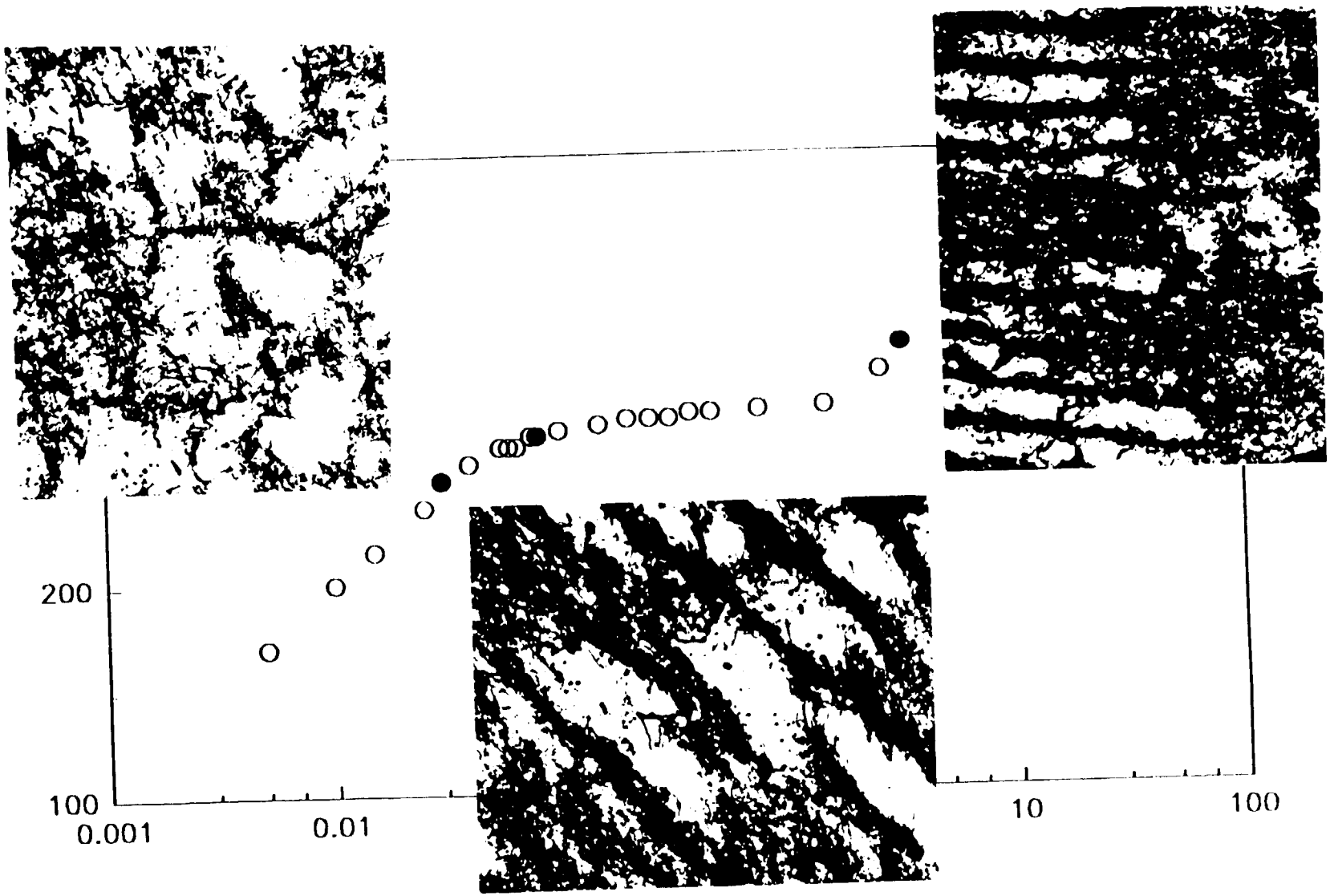


**Figure 4.21** - Cyclic hardening curve of sample tested to failure at 600 K and $\Delta\epsilon_p = 0.005$ with micrographs of the dislocation structure after (a) 5 cycles, (b) 15 cycles, and (c) failure at 781 cycles.

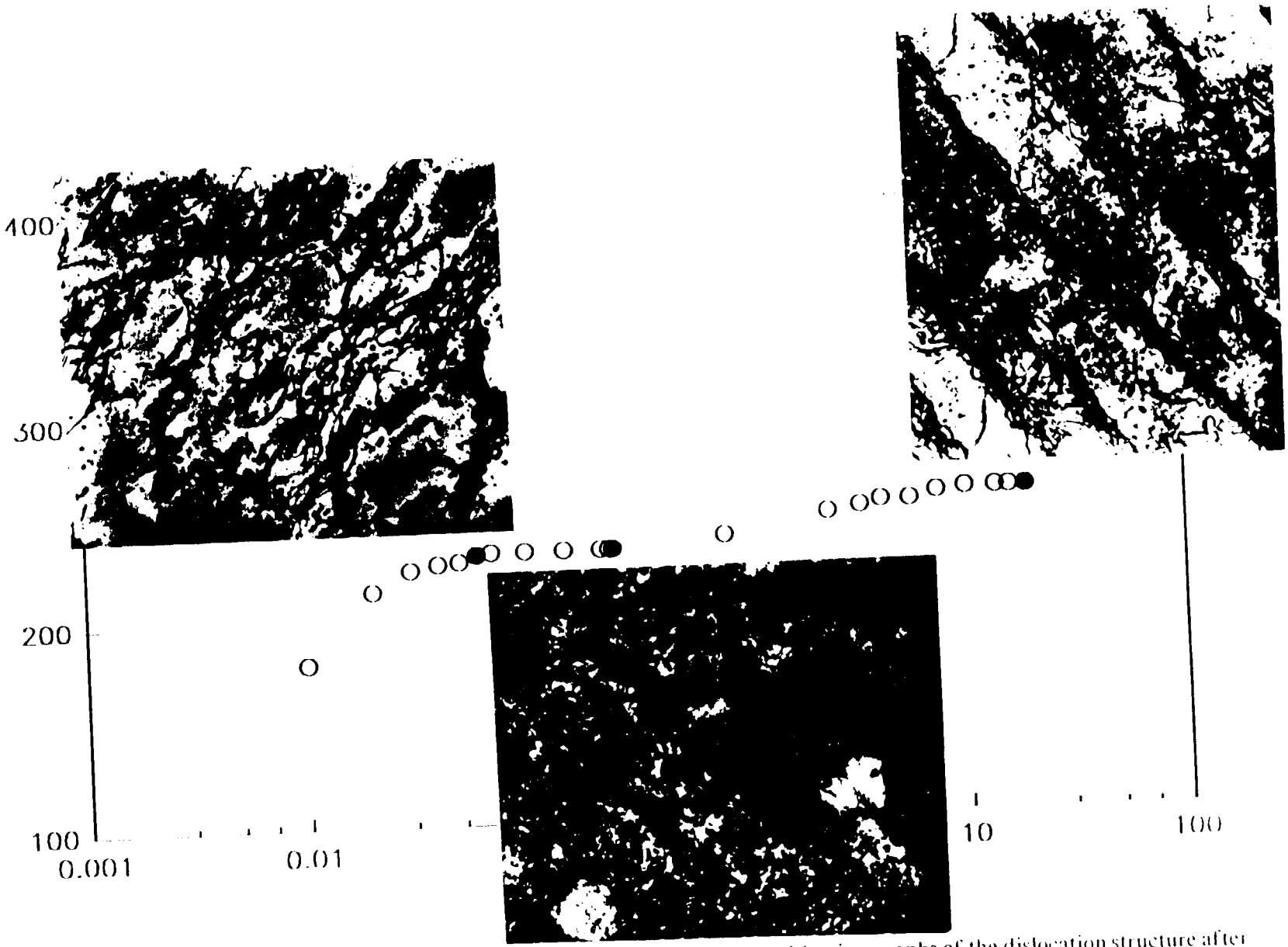


**Figure 4.22 -** Cyclic hardening curve of sample tested to failure at 700 K and $\Delta\epsilon_p = 0.01$ with micrographs of the dislocation structure after (a) 6 cycles, (b) failure at 491 cycles, and (c) failure at 1911 cycles.

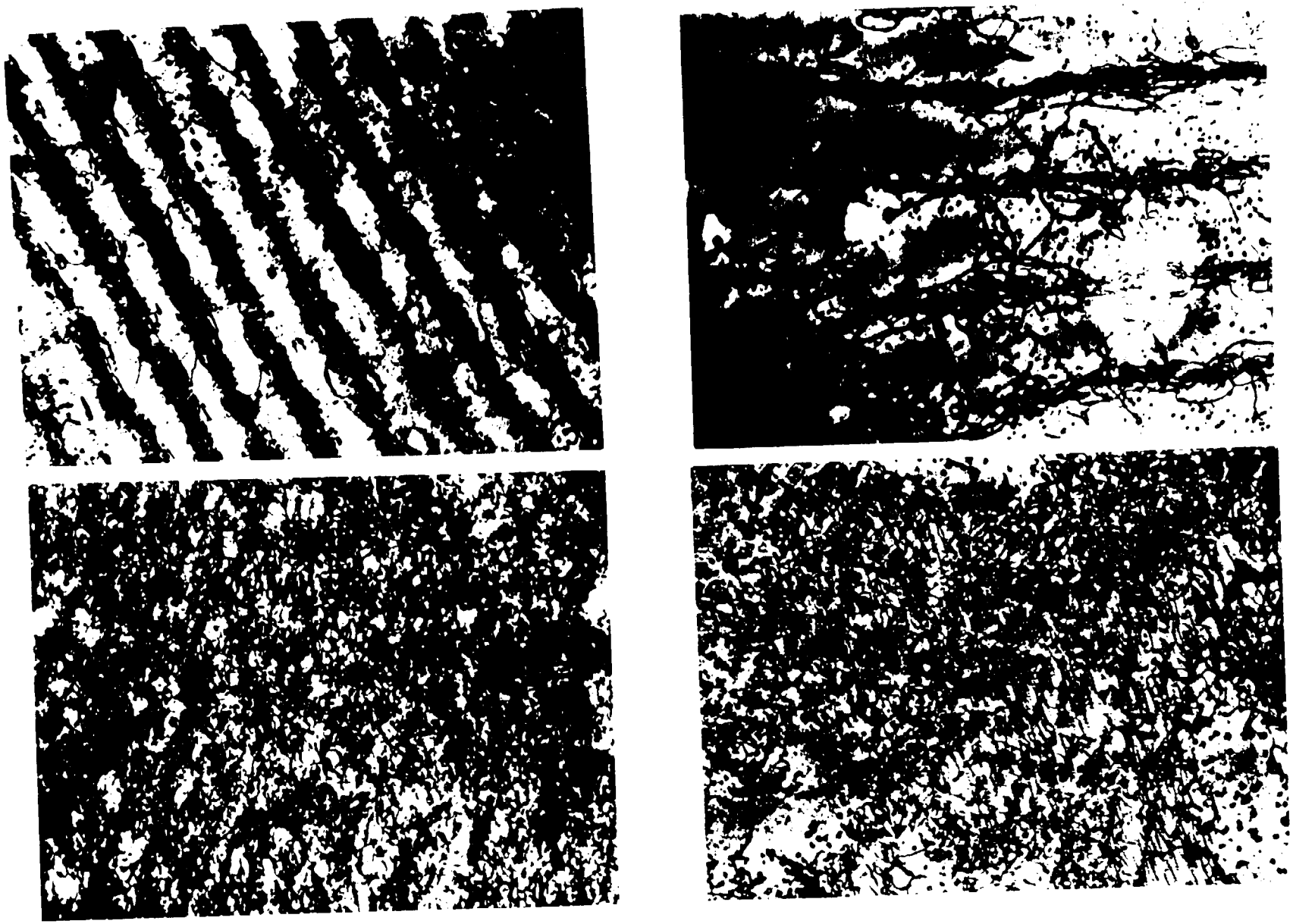


Figure 4.23 - Dislocation structures of samples tested to failure at $\Delta\varepsilon_p = 0.005$ and (a,b) 600 K, region III and (c,d) 700 K, region IV.

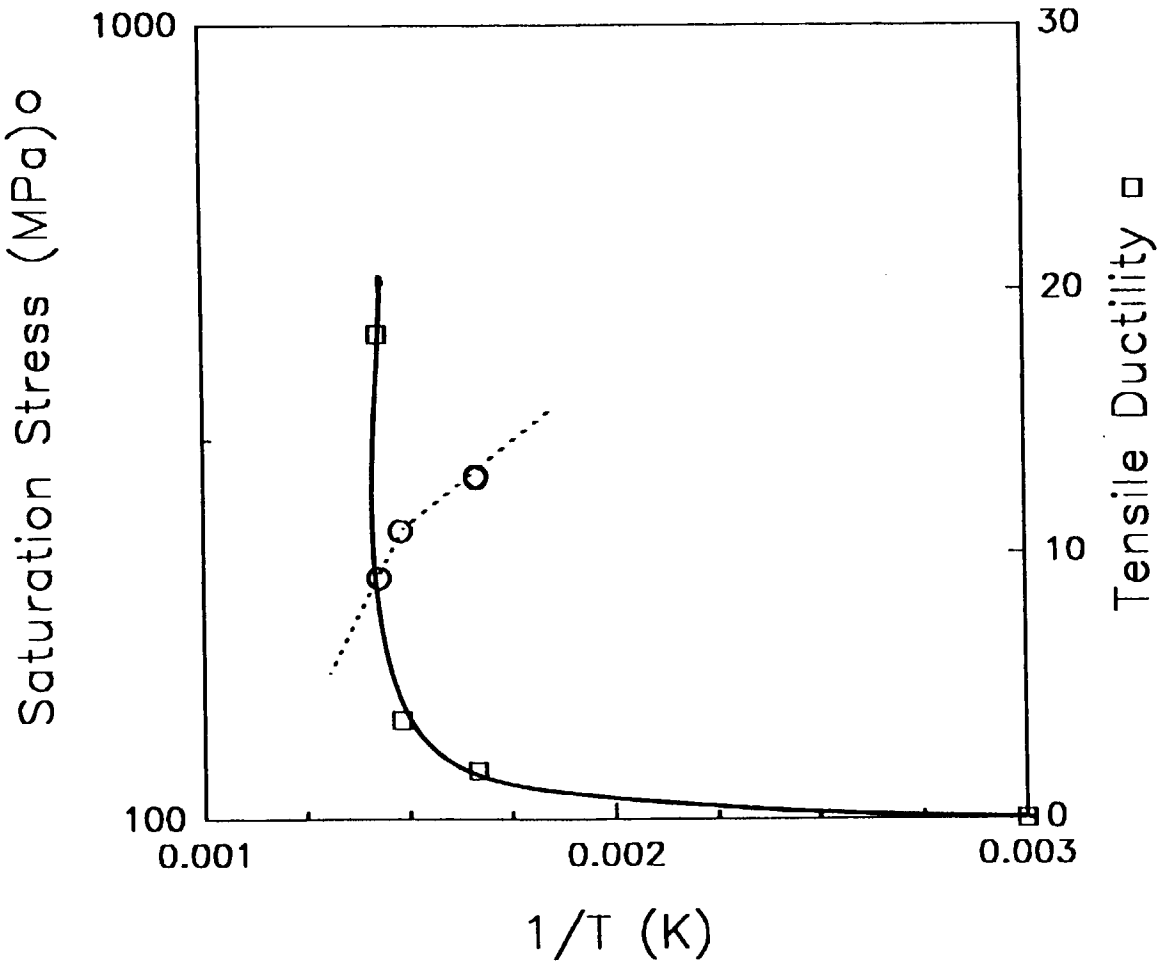


**Figure 4.24 -** Log saturation (region II) stress and monotonic ductility versus 1/T for tests conducted at $\dot{e} = 10^{-4}$ $s^{-1}$ and $\Delta e_p = 0.005$.

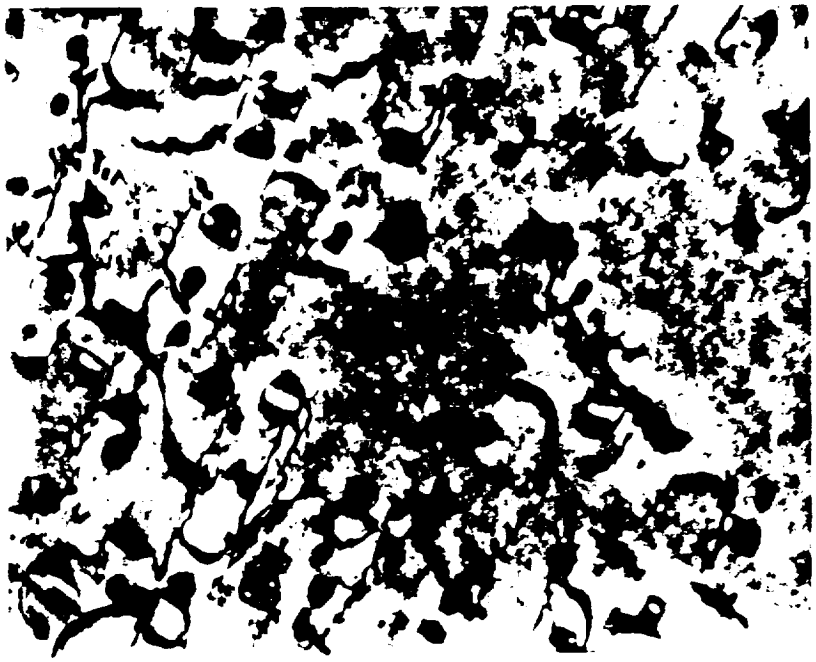


**Figure 4.25** - Regions of well aligned loops probably created superjogs of moving dislocations.